Vortex-induced vibration of a neutrally buoyant tethered sphere

H. Lee[1], K. Hourigan[1,2] and M. C. Thompson[1],†

[1]Fluids Laboratory for Aeronautical and Industrial Research (FLAIR), Department of Mechanical and Aerospace Engineering, Monash University, Melbourne, VIC 3800, Australia

[2]Division of Biological Engineering, Monash University, Melbourne, VIC 3800, Australia

A combined numerical and experimental study examining vortex-induced vibration (VIV) of a neutrally buoyant tethered sphere has been undertaken. The study covered the Reynolds-number range $50 \leqslant Re \lesssim 12\,000$, with the numerical ($50 \leqslant Re \leqslant 800$) and experimental ($370 \leqslant Re \lesssim 12\,000$) ranges overlapping. Neutral buoyancy was chosen to eliminate one parameter, i.e. the influence of gravity, on the VIV behaviour, although, of course, the effect of added mass remains. The tether length was also chosen to be sufficiently long so that, to a good approximation, the sphere was constrained to move within a plane. Seven broad but relatively distinct sphere oscillation and wake states could be distinguished. For regime I, the wake is steady and axisymmetric, and it undergoes transition to a steady two-tailed wake in regime II at $Re = 210$. Those regimes are directly analogous to those of a fixed sphere. Once the sphere begins to vibrate at $Re \simeq 270$ in regime III, the wake behaviour is distinct from the fixed-sphere wake. Initially the vibration frequency of the sphere is half the shedding frequency in the wake, with the latter consistent with the fixed-sphere wake frequency. The sphere vibration is not purely periodic but modulated over several base periods. However, at slightly higher Reynolds numbers ($Re \simeq 280$), planar symmetry is broken, and the vibration shifts to the planar normal (or azimuthal) direction, and becomes completely azimuthal at the start of regime IV at $Re = 300$. In comparison, for a fixed sphere, planar symmetry is broken at a much higher Reynolds number of $Re \simeq 375$. Interestingly, planar symmetry returns to the wake for $Re > 330$, in regime V, for which the oscillations are again radial, and is maintained until $Re = 450$ or higher. At the same time, the characteristic vortex loops in the wake become symmetrical, i.e. two-sided. For $Re > 500$, in regime VI, the trajectory of the sphere becomes irregular, possibly chaotic. That state is maintained over the remaining Reynolds-number range simulated numerically ($Re \leqslant 800$). Experiments overlapping this Reynolds-number range confirm the amplitude radial oscillations in regime V and the chaotic wandering for regime VI. At still higher Reynolds numbers of $Re > 3000$, in regime VII, the trajectories evolve to quasi-circular orbits about the neutral point, with the orbital radius increasing as the Reynolds number is increased. At $Re = 12\,000$, the orbital diameter reaches approximately one sphere diameter. Of interest, this transition sequence is distinct from that for a vertically tethered *heavy* sphere, which undergoes transition to quasi-circular orbits beyond $Re = 500$.

Key words: aerodynamics, fluid–structure interactions, vortex shedding

---

† Email address for correspondence: mark.thompson@monash.edu

1. Introduction

Vortex-induced vibration (VIV) of structures is of practical interest to many fields of engineering; for example, it can cause vibrations of heat exchanger tubes, and it influences the dynamics of offshore risers. It is important to the design of civil engineering structures such as bridges and chimneys stacks, as well as to the design of marine and land vehicles, and it can cause large-amplitude vibrations of tethered structures in the ocean. These examples number only a few of a large range of problems where VIV is important. The practical significance of VIV has led to many fundamental studies, many of which are discussed in the comprehensive reviews of Sarpkaya (1979, 2004), Griffin & Ramberg (1982) and Williamson & Govardhan (2004). As the wakes and the vortex shedding patterns of bluff bodies are closely related to VIV, the literature of the sphere at rest is to be reviewed first; the review of VIV of bluff bodies will then follow.

The wake transitions of a sphere are remarkably different from those of the circular cylinder (Johnson & Patel 1999; Tomboulides & Orszag 2000). A major difference is that the wake of a sphere becomes asymmetrical prior to a transition to unsteady flow, whereas the cylinder wake becomes unsteady before asymmetric structures appear in the wake (Williamson 1988).

Taneda (1956) performed an experimental study of the flow past a sphere being towed through a tank, for Reynolds numbers $5 < Re < 300$. By extrapolating the linear relationship between the measured recirculation bubble length and $\log Re$ to zero, he obtained a transition Reynolds number for flow separation from the sphere of $Re_{S1} = 24$, within some uncertainty due to the difficulty in identifying and quantifying small recirculation bubbles. Recent numerical computations have improved this estimate to $Re_{S1} = 20$ (Tomboulides, Orszag & Karniadakis 1993; Johnson & Patel 1999; Tomboulides & Orszag 2000), which is also consistent with an experimental study by Dennis & Walker (1971).

Natarajan & Acrivos (1993) predicted that the first bifurcation of the steady axisymmetric wake of a sphere occurred at $Re_{S2} = 210$, with an azimuthal mode number $m = 1$. This instability was predicted to occur through a regular (steady to steady flow) transition. They predicted that a secondary mode occurs at $Re_{S3} \approx 277.5$. This secondary instability was predicted to occur through a Hopf bifurcation to unsteady flow, with an azimuthal symmetry of $m = 1$. Despite the axisymmetric base flow not providing a physical representation of the wake beyond the primary non-axisymmetric instability, the predicted Hopf mode was still qualitatively consistent with the experimental observations of the onset of unsteady flow in the wake ($270 < Re_{S3} < 300$), such as the descending liquid-drop experiments of Magarvey & Bishop (1961*a*,*b*), which produced some beautiful images of the wake. In their second paper, Magarvey & Bishop (1961*b*) reported experiments over a wide Reynolds-number range $0 < Re < 2500$. Their experimental rig enabled detailed images of the trailing wakes to be obtained. Attention was paid to classifying the observed wakes, which were summarized as follows: class I ($0 < Re < 210$) exhibits a single-thread wake, class II ($210 < Re < 270$) exhibits a double-thread wake, classes III to V ($270 < Re < 700$) exhibit planar-symmetric unsteady wakes, and class VI ($Re > 700$) exhibit asymmetrical aperiodic wakes. Various experimental and numerical studies on the unsteady wake from a solid sphere show that the wake consists of vortex loops or hairpins that shed downstream from the sphere, in the same plane as that of the steady double-threaded wake (Johnson & Patel 1999; Leweke *et al.* 1999; Ormières & Provansal 1999; Ghidersa & Dušek 2000; Thompson, Leweke & Provansal 2001).

The stability of the sphere wake was studied using the complex wave amplitude Stuart–Landau equation (Ghidersa & Dušek 2000; Thompson *et al.* 2001). The coefficients of the linear and cubic terms of the Landau model were estimated from non-axisymmetric numerical computations close to the transition Reynolds numbers. The initial asymmetric transition was found to be a regular-type transition, occurring at $Re_{S2} = 212$, and the subsequent transition was identified as being a Hopf transition at $Re_{S3} = 272$. Both transitions occur through continuous supercritical bifurcations, and hence no hysteresis is expected in the vicinity of either transition. The Hopf transition in the wake of a sphere was the subject of an experimental study by Schouveiler & Provansal (2002), who verified the supercritical nature and determined Landau model coefficients experimentally.

Experiments and numerical computations performed by Johnson & Patel (1999) found the axisymmetric wake to undergo a regular bifurcation through a shift of the steady recirculating bubble behind the sphere from the axis at $Re_{S2} \approx 211$. They observed the double-threaded wake, consistent with previous experimental observations (Magarvey & Bishop 1961*a*,*b*). The numerical studies of Tomboulides *et al.* (1993) and Tomboulides & Orszag (2000) find a similar value, $Re_{S2} = 212$.

Computations by Mittal (1999*a*,*b*) showed that the wake remained planar-symmetric up to a Reynolds number of $Re \approx 375$, beyond which the planar symmetry was lost, i.e. there was flow across the plane passing between the trailing streamwise vortices. Combining a digital particle image velocimetry technique with a spatio-temporal reconstruction technique, the asymmetric structure of the wake of a sphere was analysed experimentally by Brücker (2001), who observed a similar loss of symmetry occurring within the Reynolds-number range $400 < Re < 500$.

At higher Reynolds numbers, Tomboulides *et al.* (1993) observed fine-scale flow structures in the wake of a sphere computed with a large-eddy simulation method, for a Reynolds-number range of $500 < Re < 1000$. Magarvey & Bishop (1961*b*) observed a breakdown in periodicity of the hairpin shedding for $Re > 600$ also. These results are considered to mark the onset of turbulence. Measurements indicating the development of similar fine-scale structures are reported by Chomaz, Bonneton & Hopfinger (1993) and Tomboulides & Orszag (2000), who speculated that these structures developed from a Kelvin–Helmholtz instability of the shear layer separating from the sphere. The smoke-wire visualizations presented by Kim & Durbin (1988) show fine-scale wake structures behind a sphere for $Re = 32\,000$, consistent with a Kelvin–Helmholtz instability of the separating shear layer as is observed to occur for a cylinder wake (e.g. Prasad & Williamson 1997; Thompson & Hourigan 2005).

The vast majority of work to date on tethered spheres has been concerned with the action of surface waves on tethered buoyant structures. For example, the investigations of Harlemann & Shapiro (1961) and Shi-Igai & Kono (1969) employed empirically obtained drag and inertia coefficients for use in the so-called *Morison's equation* (Morison *et al.* 1950; Sarpkaya 1986). Consequently, because the waves represented harmonic forcing functions, the tethered sphere was found to vibrate vigorously. However, the coupling of the wave motion and the dynamics of the sphere resulted in complicated equations of motion, from which it is difficult to understand the underlying physics.

Gottlieb (1997) investigated a nonlinear, small-body mooring configuration excited by finite-amplitude waves and restrained by a massless elastic tether. A Lagrangian approach was formulated in which the stability of periodic motion was determined numerically using Floquet analysis and revealed a bifurcation structure including ultra-subharmonic and quasi-periodic responses. The hydrodynamic dissipation mechanism

was found to control stability thresholds, whereas the convective terms enhanced the onset of secondary resonances culminating in chaotic motion. Consequently, excitation by finite-amplitude waves may generate a complex transfer of energy between the modes of motion for wave frequencies that are integer multiples of the system natural frequencies.

Williamson & Govardhan (1997) found that a tethered sphere does indeed vibrate in a uniform flow. In particular, they found that it will oscillate vigorously at a transverse saturation amplitude of close to two diameters peak-to-peak. This transverse oscillation frequency was at half the frequency of the streamwise oscillations, although the natural frequencies of both the streamwise and transverse motions were the same. In the Reynolds-number range of their experiments ($Re < 12\,000$), the response amplitude was a function of the flow velocity. They found that a more suitable parameter on which to gauge the response is the reduced velocity, U^*. However, conclusions regarding the synchronization of natural and vortex formation frequencies were lacking owing to the large scatter in the literature of the vortex formation frequency in the wake of a sphere.

Govardhan & Williamson (1997) noted that the maximum root-mean-square (r.m.s.) amplitude was approximately 1.1 diameters, regardless of the mass ratio. It was further found that the vortex shedding frequency for a fixed sphere matched the natural frequency for the tethered sphere at the same reduced velocity, $U^* \approx 5$, at which the local peak in the r.m.s. response occurred. This suggests that the local peak in the r.m.s. response is caused by a resonance between the natural frequency of the tethered body and the wake vortex shedding frequency, and is known as the mode I response. For high mass ratios (typically $m^* \gg 1$), the oscillation frequency at large reduced velocity tended towards the natural frequency. However, it is interesting to note that the oscillation frequency for lower mass ratios ($m^* < 1$) at high U^* did not correspond to either the natural frequency or the vortex shedding frequency for a fixed sphere.

Jauvtis, Govardhan & Williamson (2001) focused on mass ratios between $m^* = 80$ and 940, and reduced velocities in the range $U^* = 0\text{--}300$. For the sphere of mass ratio 80, they found a new mode of vibration (defined as mode III), which extends over a broad regime of $U^* = 20\text{--}40$. Because of the high mass ratios involved, the oscillation frequency remained very close to the natural frequency of the tethered sphere, whereas low m^* yielded oscillation frequencies higher than, and departing significantly from, the natural frequency (Govardhan & Williamson 1997). This mode cannot be explained as the classical lock-in effect, since between three and eight cycles of vortex shedding occur for each cycle of sphere motion. Although no explanation is given here, they note that there must exist vortex dynamics that are repeatable in each cycle, and give rise to the fluid forcing component that is synchronized with the body motion.

Jauvtis *et al.* (2001) also found that, for reduced velocities beyond the regime for mode III, another vibration mode was discovered that grew in amplitude and persisted to the limit of flow speed in the wind tunnel. The sphere dynamics of this 'mode IV' were characterized by intermittent bursts of large-amplitude vibration, in contrast to the periodic vibrations of modes I to III. In addition, despite these intermittent bursts, the vibration frequency of this mode remained very close to the natural frequency throughout the range of up to at least $U^* = 300$. With the vortex shedding frequency between 40 and 50 times the oscillation frequency, the vortex shedding cannot be responsible for these large vibrations, and the origin of these transient bursts remains unknown.

Govardhan & Williamson (2005) extended their previous study on sphere vortex-induced vibration and found that the body oscillation frequency f is of the order of the

vortex shedding frequency of a fixed body f_{vo}, and there exist two modes of periodic large-amplitude oscillation, defined as modes I and II (Govardhan & Williamson 1997; Williamson & Govardhan 1997), separated by a transition regime exhibiting non-periodic vibration. In the case of the very light tethered body, the transition between modes is quite distinct, especially when the response amplitude is plotted versus the parameter $(U^*/f^*)St$, which is equivalent to f_{vo}/f, where a jump between modes is clearly exhibited.

Govardhan & Williamson (2005) also noted that the phase of the vortex force relative to sphere dynamics is quite different between the modes I and II. This difference in the phase of the vortex force is consistent with the large difference in the timing of the vortex formation between modes, which was observed from the vorticity measurements for the light-sphere vibrations.

Pregnalato (2003) numerically investigated the case of a tethered sphere for the much lower Reynolds-number range, $200 \geqslant Re \geqslant 500$. In his investigation, the first mode of oscillation, mode I, found by Govardhan & Williamson (2005), was not found. However, the numerical results compared well with experiments performed in the same Reynolds-number range.

Provansal, Schouveiler & Leweke (2004) examined the trajectories of a vertically tethered heavy sphere. For a mass ratio of 2.433, they observed quasi-circular or elliptic motion in a plane normal to the flow for the Reynolds-number range $600 \leqslant Re \leqslant 800$. This contrasts with the types of motion observed for the cases discussed above, with horizontal flow and with gravity acting vertically. In addition, from numerical simulations, Behara, Borazjani & Sotiropoulos (2011) found circular oscillations and a spiral wake mode for an $m^* = 2$ elastically mounted sphere with three degrees of freedom at $Re = 300$, for values of reduced velocity in the range $4 \leqslant U^* \leqslant 9$. In that case it was found that different sphere motions were observed at the same reduced velocity.

The aim of the current study is to quantify the different oscillation regimes of a neutrally buoyant tethered sphere as a function of the Reynolds number. The neutrally buoyant case was chosen to eliminate the effects of buoyancy and gravity on the motion in order to provide a reference case for the more complex situation when the influence of gravity is included. From that point of view, there are some similarities to the numerical simulations of Behara *et al.* (2011), for which the sphere of $m^* = 2$ was allowed to move in three dimensions constrained by linear springs without the effect of gravity. For the case here, neutral buoyancy and possibly the restriction to movement on a two-dimensional spherical surface lead to a different set of trajectories and, in particular, to the onset of circular motion being delayed to much higher Reynolds numbers.

This paper is organized as follows. The underlying mathematics is presented first. Following this, the computational method is discussed, including validation and grid resolution studies, and the experimental method is described. Results are then presented in terms of key parameters controlling the body oscillation and wake characteristics, including oscillation frequency, amplitude and trajectory, wake symmetries and structures, and phase behaviour. A summary of the different regimes is provided before presenting the conclusions.

2. Problem formulation

The tethered-sphere system is sketched in figure 1. The forces acting on the sphere are the tether tension T, buoyancy force B, body weight W, streamwise fluid force F_x,
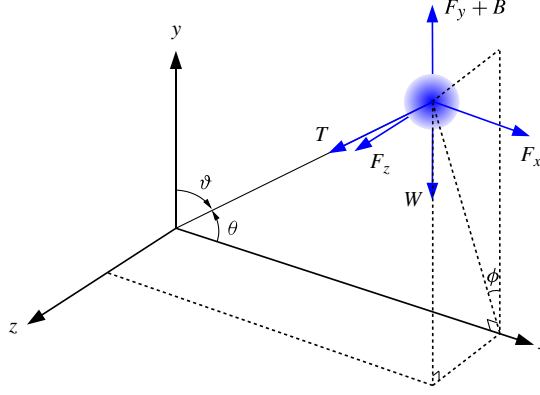
FIGURE 1. (Colour online) Coordinate system and forces on a tethered sphere.

transverse fluid force F_y and lateral fluid force F_z. Fluid flows past the sphere in the positive x direction.

The tension is linked to the other force components by

$$T = F_x \cos\theta + (F_y + B - W) \sin\theta \cos\phi + F_z \sin\theta \sin\phi, \qquad (2.1)$$

where the tether angle θ is the angle to the sphere from the streamwise (x) axis, and ϕ is the inclination angle of the sphere in the cross-flow (yz) plane. This is just a statement of radial force balance. The tether angle (θ) plus the layover angle (ϑ) of Williamson & Govardhan (1997) equals $90°$.

The equations of motion for the sphere are given by

$$m\ddot{x} = F_x - T \cos\theta, \qquad (2.2)$$
$$m\ddot{y} = (F_y + B - W) - T \sin\theta \cos\phi, \qquad (2.3)$$
$$m\ddot{z} = F_z - T \sin\theta \sin\phi. \qquad (2.4)$$

Here $m = (4/3)\pi(D^3/8)\rho_b$ is the mass of the sphere, with ρ_b its density and D the diameter of the sphere.

By substituting for the tension from (2.1) and converting to Cartesian coordinates, these equations can be reduced to

$$\frac{\ddot{x}}{\gamma} = \frac{1}{m^*} \left\{ \left[1 - \left(\frac{x}{L} \right)^2 \right] C_x - [C_y + (1 - m^*)\alpha] \frac{y}{L}\frac{x}{L} + C_z \frac{z}{L}\frac{x}{L} \right\}, \qquad (2.5)$$

$$\frac{\ddot{y}}{\gamma} = \frac{1}{m^*} \left\{ \left[1 - \left(\frac{y}{L} \right)^2 \right] [C_y + (1 - m^*)\alpha] - C_x \frac{x}{L}\frac{y}{L} + C_z \frac{z}{L}\frac{y}{L} \right\}, \qquad (2.6)$$

$$\frac{\ddot{z}}{\gamma} = \frac{1}{m^*} \left\{ \left[1 - \left(\frac{z}{L} \right)^2 \right] C_z - C_x \frac{x}{L}\frac{z}{L} + [C_y + (1 - m^*)\alpha] \frac{y}{L}\frac{z}{L} \right\}. \qquad (2.7)$$

The parameters appearing in (2.5)–(2.7) are:

  (i) the drag coefficient $C_x = F_x/(\rho_f A U^2/2)$;
 (ii) the lift coefficient $C_y = F_y/(\rho_f A U^2/2)$;
(iii) the side force coefficient $C_z = F_z/(\rho_f A U^2/2)$;
(iv) the mass ratio $m^* = \rho_b/\rho_f$;

(v) a Froude number $\alpha = 4gD/3U^2$, and

(vi) a dimensional acceleration $\gamma = 3U^2/4D$.

In addition, ρ_f is the fluid density, U is the upstream flow speed, L is the inextensible tether length and $A = \pi D^2/4$ is the cross-sectional area of the sphere. Note that the tether causes the sphere to move on a spherical surface of radius L.

These equations are solved together with the incompressible Navier–Stokes equations as a coupled system in an accelerating frame of reference attached to the centre of the sphere. The Reynolds number is given by $Re = UD/\nu$, with ν being the kinematic viscosity.

3. Computational method

3.1. *Time integration*

For the fluid calculation, a second-order, three-step, time-splitting scheme was employed to evolve the fluid velocity and pressure fields. The three steps account for the convection, pressure and diffusion terms of the incompressible Navier–Stokes equation. In the first of the three steps, the convection term was evaluated using a third-order Adams–Bashforth scheme (and semi-implicit Adams–Moulton scheme in subsequent iterations). Then, the pressure field was evaluated by forming a Poisson equation by taking the divergence of the equation for the pressure, and enforcing continuity at the end of the step. The diffusion term was evaluated with the theta form of the Crank–Nicolson scheme. This results in a Helmholtz equation. Both the Poisson equation for the pressure and the Helmholtz equations for the viscous terms lead to linear matrix problems, once the equations are discretized in space, as described below. The matrices are inverted at the start of the time-stepping procedure; subsequently, the effects of continuity (pressure) and viscous diffusion at each time step only involve matrix multiplications. Because the convection term is nonlinear, it is generally treated explicitly. The pressure boundary condition is treated using the approach described in Karniadakis, Israeli & Orszag (1991), leading to a second-order time-accurate velocity field, which has been verified using convergence tests. For the VIV case, there is strong coupling between the fluid and the structural response. The explicit approach becomes unstable and the overall time stepping has to be treated semi-implicitly.

To commence the time-stepping procedure, the sphere position at the end of the time step is first predicted from straight extrapolation from stored positions at previous time steps. Then the fluid variables, i.e. the velocity and pressure fields, are updated using the three-step method described above. At this stage, the position and velocity of the sphere are updated. The finite-difference time-stepping procedure for the motion of the sphere is based on the leapfrog approach, with the velocity of the sphere calculated halfway through the time step using the current calculated surface forces and two stored force vectors at previous time steps. This provides a third-order velocity prediction. Then the displacement vector at the end of the time step is updated using a third-order time-stepping method based on this calculated velocity and the two previous stored velocity vectors. Under-relaxation can be used for the velocity update while iterating for a single time step, i.e. only part of the predicted velocity change is added during each iteration. The under-relaxation parameter required is dependent on the mass ratio and somewhat on the Reynolds number, but typically the value needs to be less than unity to ensure convergence when the mass ratio is small (i.e. $m^* \leqslant 0.5$). It is not required for simulations described in this paper. At this stage, the iteration loop returns to the fluid calculation, but now it is based on the newly calculated position of the sphere. Once again, the sphere velocity and position are updated. Then

convergence is tested by comparing the differences in the force on the sphere, and the velocity of the sphere, between iterations, together with the maximum fluid velocity change over all grid points between iterations. Iteration continues until convergence and then moves to the next time step. The convergence tolerances were adjusted until any further tightening produced no change in the results. Typically, it takes two or three inner iterations to establish convergence, but perhaps a few more at the start of each simulation; however, the time step can generally be chosen to be up to an order of magnitude greater than a time step based on the Courant condition. Further details on the basic approach can be found in Thompson *et al.* (2006).

3.2. *Spatial discretization*

The three-dimensional fluid equations are discretized using a spectral element–Fourier spectral method with a global Galerkin Fourier spectral discretization in the third dimension, which is the azimuthal direction in the present study. This has been employed previously for the case of the flow past a circular cylinder by Karniadakis & Triantafyllou (1992) and Thompson, Hourigan & Sheridan (1996). The spatial discretization consists of F equi-spaced planes in the azimuthal direction, each consisting of an identical spectral-element mesh in two dimensions (streamwise and transverse directions). The flow variables are transformed into Fourier space in the azimuthal direction for each node on the spectral-element mesh using a fast Fourier transform. This decouples the problem into a set of F equations for each Fourier mode, which are then solved independently for the linear operators. The spatial domain in the streamwise and transverse directions was discretized into a number of macro-elements, with the majority concentrated in the wake and boundary layer regions. Domain size and resolution studies were conducted to validate the predictions. Within each element, the mesh geometry as well as the velocity and pressure fields, were represented by up to eighth-order tensor-product polynomials, associated with Gauss–Lobatto–Legendre quadrature points. Details of the approach and implementation have been provided by Thompson *et al.* (1996), Leontini, Thompson & Hourigan (2007) and Ryan, Thompson & Hourigan (2007). First-order boundary conditions (Karniadakis *et al.* 1991) are used for the pressure gradient at the sphere surface and far-field boundaries. At the outlet the pressure is fixed and the normal velocity gradient is set to zero. The fluid equations are solved in a non-inertial moving-frame Cartesian coordinate system $(x'y'z')$ attached to the sphere, whereas the motion of the sphere is calculated in the fixed Cartesian frame (xyz). Because of the rigid tether, the sphere actually rotates during its motion. That motion is taken into account to set velocity and pressure boundary conditions in the moving frame at the surface of the sphere.

3.3. *Validation*

A validation study for the tethered-sphere VIV was initially performed. Using experience gained from previous studies on fixed and oscillating spheres (Thompson *et al.* 2001; Leweke, Thompson & Hourigan 2006; Thompson, Leweke & Hourigan 2007; Stewart *et al.* 2010), a set of meshes were constructed. The key fluid properties and sphere motions for different domain sizes and the grid resolutions were compared to determine an acceptable mesh to generate accurate and computationally practicable solutions.

3.3.1. *Mesh independence study*

   The three meshes shown in figure 2 were used to validate the numerical results. In particular, S1 is constructed after an extensive search of the literature dealing with

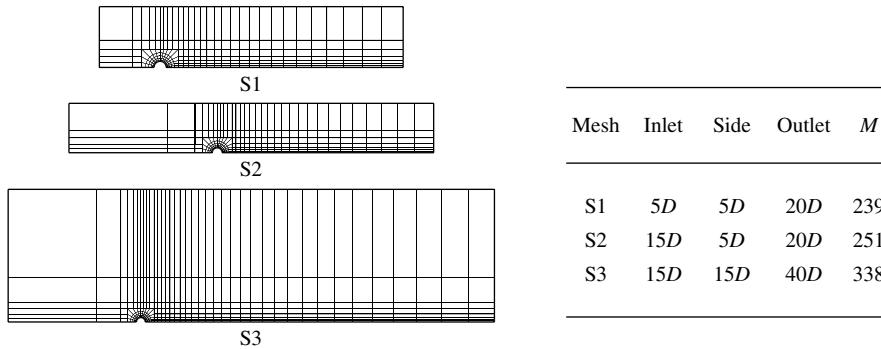| Mesh	Inlet	Side	Outlet	M
S1	$5D$	$5D$	$20D$	239
S2	$15D$	$5D$	$20D$	251
S3	$15D$	$15D$	$40D$	338

FIGURE 2. Meshes examined for the tethered-sphere simulations.

the flow simulations around a sphere. From the literature, it was reported that, for simulations of a fixed sphere in free stream, changing the inlet extent and radial extent from $5D$ to $10D$ resulted in minimal differences in measured flow properties (Tomboulides & Orszag 2000; Pregnalato 2003). In addition, it was also reported that predictions based on outflow domain lengths of $20D$ and $40D$ also showed negligible differences (Ghidersa & Dušek 2000; Tomboulides & Orszag 2000). Based on these results, the radial and inlet extents of the mesh S1 were set to $5D$, and the outlet length set to $20D$. Formally, this results in a blockage ratio of 4 %. The adequacy of this computational domain size is considered further below.

Some care was taken in choosing the element size close to the sphere. The normal extent of elements adjacent to the sphere was chosen according to the boundary layer thickness for axisymmetric laminar boundary layers. From estimates of the boundary layer thickness, the required size of the elements was derived based on the analysis of Gottlieb & Orszag (1977) and Tomboulides & Orszag (2000) for spectral-based methods. Accordingly, the element thickness of all meshes was set to $0.1D$, which should maintain acceptable accuracy down to an internal element polynomial order of 4 for $Re = 1000$.

The larger meshes S2 and S3 were used to examine whether mesh S1 imposes unacceptable blockage. These meshes were constructed from the S1 mesh by adding elements to have increased inflow, outflow and radial extents. The domain sizes of each of these meshes are given in figure 2.

At $Re = 300$, the flow past a stationary sphere is unsteady and characterized by the presence of periodically shed vortex loops. In addition, the tethered sphere shows a near-periodic oscillation around its mean radial position, with an amplitude of approximately $0.08D$. Note that the oscillation amplitude in the periodic regime ($Re \leqslant 500$) is limited to be below approximately $0.12D$. This case was used to examine the domain size effects, by recording the mean value of the tether angle and the radial oscillation amplitude on the three meshes. The results are shown in table 1. This indicates that, for mesh S1, the mean tether angle lies within 4 % of the values on the larger meshes, and the amplitude varies by less than 2 %. Thus, in terms of blockage, mesh S1 appears to be sufficiently large to provide acceptable accuracy and to capture the flow physics, and it was used for all simulations presented in this paper.

Mesh	θ (deg.)	A_{tot}^*		$N \times N$	C_x	C_y	C_z
S1	4.12	0.0346		5×5	0.679	−0.0207	0.057
S2	3.98	0.0351		6×6	0.677	0.0025	0.062
S3	4.11	0.0348		7×7	0.677	0.0027	0.061
				8×8	0.677	0.0027	0.061
				9×9	0.678	0.0028	0.061

TABLE 1. Left: Domain size study results. Here, θ is the tether angle and A_{tot}^* is the sum of the normalized amplitudes in all three directions. The results are for the tethered sphere with $m^* = 1.0$ and $10D$ tether length at $Re = 300$. These are time-mean values. Right: Resolution study results. Streamwise fluid force coefficient C_x, transverse fluid force coefficient C_y and lateral fluid force coefficient C_z as a function of number of internal nodes within each element. The results are for a tethered sphere with $m^* = 1.0$ and $10D$ tether length at $Re = 300$. Coefficients are time-mean values.

3.3.2. *Grid resolution study*

Having checked the adequacy of the computational domain size, the resolution of the mesh required to fully resolve the flow was next determined by changing the order of the Lagrange polynomial interpolants within the macro-elements. Again, the study was carried out at $Re = 300$ for an inelastically tethered sphere (as before). As a point of comparison, the mean force coefficients in each direction were calculated.

Table 1 also shows results from the resolution study. This indicates that the acceptable convergence is achieved for $N \times N = 6 \times 6$ corresponding to polynomial order $p = N - 1 = 5$. The predictions for mean force coefficients C_x and C_z lie within 1 % or better of the higher-resolution predictions. Thus, the majority of simulations for the tethered sphere were performed using fifth-order ($p = 5$) tensor-product Lagrange polynomial interpolants within elements. For Reynolds numbers higher than 300, however, it was found necessary to increase the p value to $p = 6$ for $Re = 500$ and to $p = 8$ for $Re = 800$ in order to provide this level of accuracy.

Having undertaken these studies to determine a suitable computational mesh in the streamwise–radial plane, the question of azimuthal resolution needs to be addressed. This was examined by altering the number of Fourier planes in the azimuthal direction. Ghidersa & Dušek (2000) showed that six Fourier modes, i.e. 12 Fourier planes, were sufficient to capture the secondary instability at $Re \simeq 275$. However, the breaking of planar symmetry for $Re \geqslant 375$ means that more modes are likely to be required to accurately resolve the shed vortices, not only because they shed asymmetrically but also because they are coupled with the motion of the sphere. Therefore, together with the need for additional resolution to handle an increase of Re up to 800, 24 Fourier planes were selected. Other studies have shown this resolution to be sufficient (Tomboulides & Orszag 2000). Nevertheless, to confirm that this was sufficient, force coefficients were calculated for 24 and 32 planes at $Re = 500$. The difference in force coefficient predictions was less than 1 %, which confirms that this resolution is sufficient.

4. Experimental method

A parallel experimental study was undertaken especially to examine the flow at higher Reynolds numbers but overlapping the Reynolds-number range of the numerical study. The experiments were performed in a recirculating free-surface water channel.
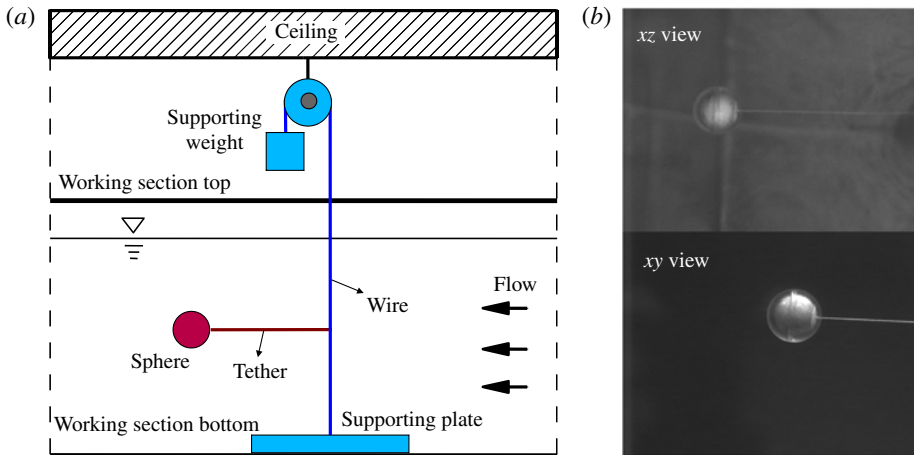
FIGURE 3. (Colour online) (*a*) Schematic of the experimental set-up and (*b*) sample images from the experiment.

Upstream of the working section, water flows through a honeycomb and a thin wire mesh before going through a two-dimensional 9 : 1 contraction to the working section. The combination of the screens and the contraction yield a measured turbulence level of less than 1.0 %. The schematic of the experimental set-up is shown in figure 3(*a*) (see Lee, Thompson & Hourigan 2008 for further details).

Spheres of diameters of 9, 16, 25 and 40 mm made of Perspex were used for the experiments. These were manufactured to allow them to be separated in half and hollowed out to allow their buoyancy ratio to be adjusted by putting material inside. In every experiment, packing material was carefully weighed and inserted to set the mass ratio to a specified value. A thin string consisting of inelastic non-twist fishing line with the diameter of 0.1 mm was carefully connected to the sphere as a tether, which was then attached to a 0.315 mm wire. The wire was vertically tensioned between the bottom of the working section and the ceiling vertically above to provide rigid supports. The wire tension required to suppress vibration was calculated and applied. To minimize the effect of vortex shedding of the wire, visual observations and preliminary video analysis of a moving sphere with a thicker wire of 0.5 mm and a thinner wire of 0.15 mm were performed. Based on this observation, it was expected that the effect of wire vortex shedding on the sphere movement is negligible, although some of the higher Reynolds-number experiments ($Re > 5000$) were above the threshold of vortex shedding for the support wire.

Animations of the motion of the sphere in both the *xy* and *yz* planes were captured using either or both a MiniDV video camera of standard resolution (720×576) operating at 25 frames per second (fps), or a higher-resolution PCO charge-coupled device camera of resolution 1360×1024 pixels, using 2, 4 or 8 fps. The recorded videos were converted to uncompressed avi files, and then each frame from the avi files was extracted for further processing. Sample images are shown in figure 3(*b*).

Two different techniques were used to extract the position of the sphere recorded in the images. For the first, which was used for most of the analysis, raw bitmap information from each video frame was used without filtering techniques. The post-processing procedure consisted of three steps. In the first step, the diameter of the sphere in an image (usually the first of the images) and the position of its centre were

identified and saved. In the second step, the number of bright pixels within a circle of the sphere diameter using the previously calculated position of the sphere centre was calculated. In the third step, an optimization function was used to update the actual position of the sphere centre, which maximized the number of bright pixels within the circle. An alternative method was used for analysis of images for experiments with the smallest sphere. In that case, it was found that the method just described was not sufficiently accurate given the relatively small movements involved. Images were first filtered so that any pixels below a certain intensity level were zeroed. This was used to make the background purely black. Careful thresholding could also remove the tether from the video frames, leaving only the image of the sphere. Then each frame was cross-correlated with the first frame in the sequence. By accurately determining the maximum of the cross-correlation function, the movement of the sphere between video frames could be resolved to subpixel accuracy.

Naturally, the first method is valid only when the image has a simple background and circular object within it. To improve image contrast for processing, two or three spotlights were set up to focus on the moving sphere during the experiments. This approach was found to be adequate to extract the sphere centre and size accurately, and was applied to process the experimental images. Typically, the sphere diameter is 100 pixels or more and the sphere position can be reliably determined within better than 2 pixels, giving a relative error of better than 2%. For the smallest sphere of diameter 9 mm, the cross-correlation technique was used to determine movement between video frames. In that case, the sphere diameter was only 30 pixels in the yz plane, so subpixel resolution was necessary to extract the trajectories accurately. These procedures were performed using specially written Matlab code using its image processing and optimization libraries. Each procedure was tested on a set of bitmap image data by comparing the identified centre and boundary of the sphere with those through visual identification for all images from one of the sequences.

5. Results

This study reveals that a neutrally buoyant tethered sphere experiences seven different identifiable flow regimes for $Re \lesssim 12\,000$. The first six regimes were identified from numerical simulations and the seventh was found through experiments at higher Reynolds numbers.

The simulations were performed on computer clusters using a parallel version of the software for $50 \leqslant Re \leqslant 800$. Some simulations have been run over 5000 non-dimensional time units (i.e. of the order of 500 oscillation cycles) to reach the asymptotic state. Reynolds numbers for the simulations were selected within this range in steps of $\Delta Re = 50$, and further simulations were performed at intermediate Reynolds numbers if a difference in body dynamics was observed between neighbouring simulations. For example, this led to running simulations at $Re = 205$, 210, 270, 280 and 330 to capture transitions between regimes more accurately.

The tether length was chosen as $10D$ for all cases. Since the yz motion is restricted to an amplitude of approximately $0.25D$, even at the upper end of the Reynolds-number range simulated, this limits the horizontal range of movement, owing to the tether constraining the motion to a spherical surface, to be approximately $0.003D$ or generally much less. Thus, to a good approximation, the motion effectively takes place within the yz plane passing through the neutral point.

Experiments were carried out to support the numerical findings and to expand the Re range beyond the limit of the numerical simulations. The experiments covered the
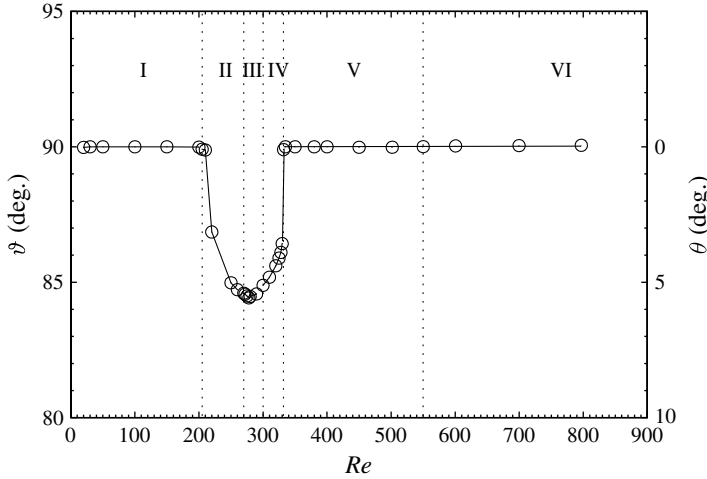
FIGURE 4. Layover angle of a neutrally buoyant sphere as a function of Reynolds number obtained from the numerical simulations.

range of $370 \leqslant Re \lesssim 12\,000$, which extends well past the range for the numerical study. But, importantly, this range overlaps the Re range for the numerical simulations.

For cases when the mean position of the sphere was not located on the x axis, i.e. the layover angle was not $90°$, the raw trajectories were first rotated about the x axis so that the mean position was located in the first quadrant of the xy plane. After this rotation, motion in the y direction corresponds to radial motion, and motion in the z direction corresponds to 'azimuthal' motion. Despite there being no difference between movement in these (Cartesian) directions when the mean position is located directly downstream on the x axis, this is not strictly the case when the mean position is not on the x axis. In that case, y (or radial) motion moves the sphere slightly upstream and downstream over an oscillation cycle, while z (or azimuthal) motion maintains the sphere at approximately the same downstream position during an oscillation cycle. When the mean position did lie on the x axis, the trajectories were still rotated, but in this case to align the largest oscillatory motion with the xy plane, again so that motion in the y direction could be associated with radial motion. For each simulation, the oscillation behaviour in y and z were used to determine the mean radial and azimuthal oscillation amplitudes and frequencies. The mean layover angle was also determined. Together, these parameters were used to classify the different flow responses as the Reynolds number was varied.

5.1. *Time-mean position: layover angle ϑ*

The angle measured from the transverse (x) axis to the centre of the body is used to represent the time-mean position of the body. This angle ϑ, which is known as the layover angle, has been used in the previous studies of VIV of tethered bodies. The layover angle for the range of $50 \leqslant Re \leqslant 800$ from the numerical simulations is shown in figure 4.

In the first regime (regime I), the sphere remains on the pivot axis without movement. The applicable Reynolds-number range is $Re \leqslant 210$. The second regime (regime II), starting at $Re \simeq 210$, is also steady but axisymmetry is lost. The wake
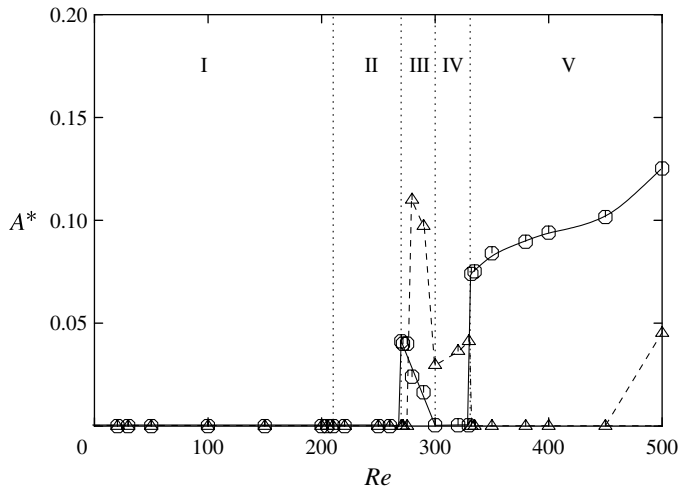
FIGURE 5. Amplitude of oscillation for a neutrally buoyant sphere from the numerical simulations. The solid line (with circles) indicates the amplitude in the radial (or *y*) direction. The dashed line (with triangles) shows the amplitude in the azimuthal (or *z*) direction.

corresponds to the two-threaded wake of a stationary sphere as observed by Magarvey & Bishop (1961*b*) and Johnson & Patel (1999). Over this range, the sphere is located offset from the symmetry axis, and the layover angle decreases from 90° as the Reynolds number is increased. This is due to the net fluid force from the non-axisymmetric two-tailed wake. This regime exists for $Re < 270$. As Re is increased further, the sphere starts to vibrate at $Re \geqslant 270$, the start of regime III. Similarly, this corresponds closely to the Reynolds number at which shedding commences for a fixed sphere. Regime IV begins at $Re = 300$. It is associated with the layover angle increasing back towards 90°. In regime V ($332 \leqslant Re \leqslant 500$), the layover angle remains close to 90°, indicating that the body oscillates symmetrically around the x' axis.

5.2. *Amplitude and frequency of oscillation*

Figure 5 shows the maximum radial and azimuthal amplitudes, A_r^* and A_θ^*, of the sphere oscillations, whereas figure 6 gives the corresponding non-dimensionalized frequencies in terms of Strouhal numbers, $St_r = f_r D/U$ and $St_\theta = f_\theta D/U$, after the asymptotic states have been reached. Sphere oscillation occurs from regime III onwards, starting from $Re = 270$. Simulations performed at the neighbouring Reynolds numbers of $Re = 265, 268, 272$ and 275 showed that the oscillation is first detectable at $Re = 270$. This is very close to the onset of wake oscillation for a fixed sphere, which has been determined as $Re_{S3} = 271$ or 272 (Johnson & Patel 1999; Ghidersa & Dušek 2000; Thompson *et al.* 2001). This indicates that the ability of the sphere to move does not appear to lead to the premature onset of wake unsteadiness.

For this regime, initially the sphere oscillates along a radial line through the neutral point. The oscillation is not strictly periodic, with the mean sphere position moving slightly radially inwards and outwards over several oscillation cycles. This is shown in figure 7(*a*). The radial amplitude of oscillation at $Re = 270$ is approximately $0.04D$.
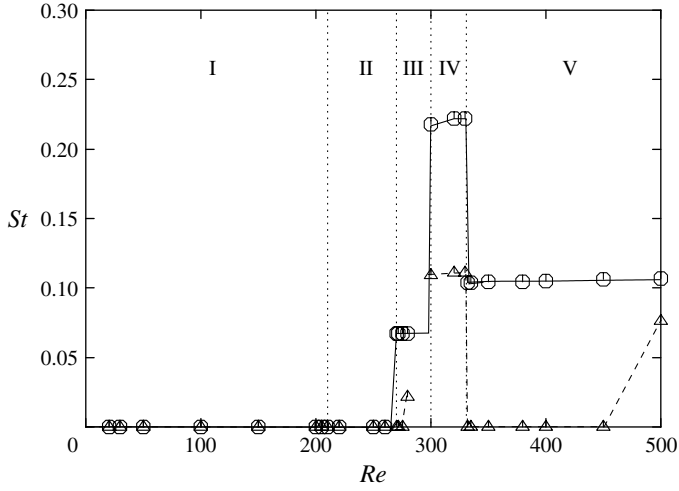
FIGURE 6. Radial and azimuthal oscillation frequencies for a neutrally buoyant sphere as a function of Reynolds number obtained from the numerical simulations.
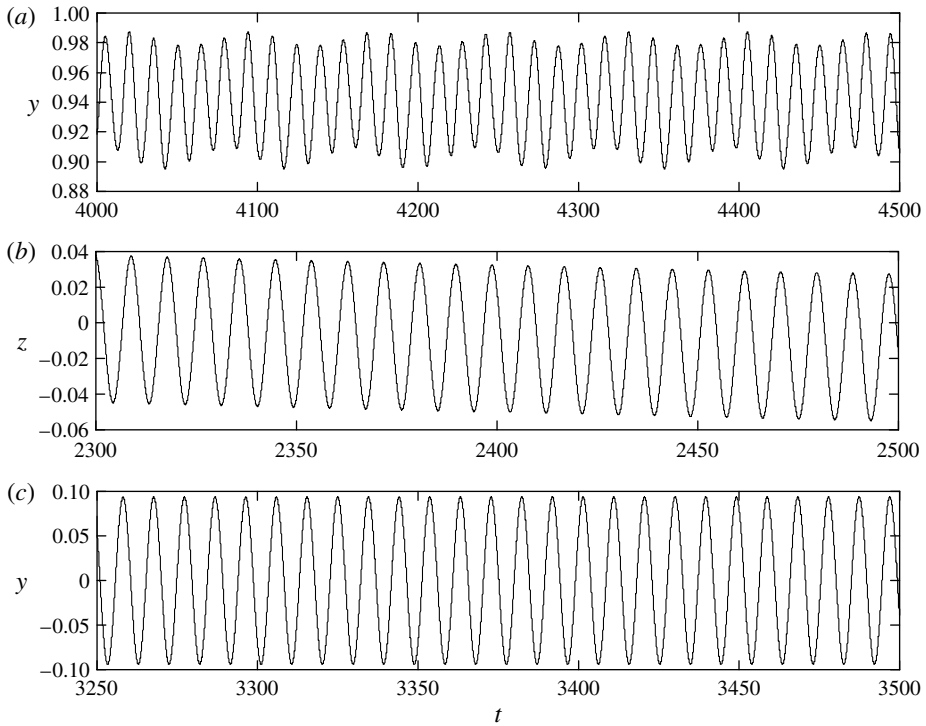

FIGURE 7. Oscillation behaviours for a neutrally buoyant sphere: (*a*) radial oscillation at $Re = 270$; (*b*) azimuthal oscillation at $Re = 330$; and (*c*) radial oscillation at $Re = 400$.

The non-dimensional natural frequency of oscillation, St_n, can be expressed as

$$St_n = \frac{f_n D}{U} = \frac{1}{2\pi}\sqrt{\frac{3}{4}\frac{\sqrt{C_x^2 + [(1 - m^*)\alpha + C_y]^2 + C_z^2}}{(C_A + m^*)L^*}}. \tag{5.1}$$

In this equation, m^* is the mass ratio, L^* is the non-dimensionalized tether length, α is the parameter defined in §2 and C_A is the added mass coefficient ($C_A = 0.5$ for a sphere) of an ideal flow.

This equation is derived from the following momentum balance equations (5.2)–(5.4):

$$(m + m_a)\ddot{x} + \frac{T}{L}x = F_x, \tag{5.2}$$

$$(m + m_a)\ddot{y} + \frac{T}{L}y = F_y + B - W, \tag{5.3}$$

$$(m + m_a)\ddot{z} + \frac{T}{L}z = F_z. \tag{5.4}$$

From these equations, it is obvious that the natural frequency is the same in all three dimensions, and is given by

$$f_n = \frac{1}{2\pi}\sqrt{\frac{T}{(m + m_a)L}}. \tag{5.5}$$

This dimensional natural frequency can be put in non-dimensional form, which is given by

$$St_n = \frac{f_n D}{U} = \frac{1}{2\pi}\sqrt{\frac{D^2}{U^2}\frac{T}{(m + m_a)L}}. \tag{5.6}$$

Substituting the expression for the tension in the tether, collecting terms and using the non-dimensional form of the fluid forces results in (5.1).

Williamson & Govardhan (1997) used (5.6) to calculate St_n by assuming that the y force, C_y, and the z force, C_z, are much smaller than the buoyancy, $(1 - m^*)\alpha$, to give

$$St_n \simeq \frac{f_n D}{U} \approx \frac{1}{2\pi}\sqrt{\frac{3}{4}\frac{\sqrt{C_x^2 + [(1 - m^*)\alpha]^2}}{(C_A + m^*)L^*}}. \tag{5.7}$$

Using (5.1), the non-dimensionalized natural frequency St_n was calculated to lie in the range of $0.0254 \leqslant St_n^* \leqslant 0.0296$. In turn, this means that the reduced velocity, $U^* = 1/St_n$, lies in the range $34 \leqslant U^* \leqslant 39$ for the numerical simulations, which covered $Re \leqslant 800$. Between $Re = 10^3$ and 10^4, the drag coefficient is approximately constant at $C_x \simeq 0.4$. Thus the reduced velocity for the experimental results was close to $U^* \simeq 44$ over most of the Reynolds-number range considered. Figure 6 shows that St_r for regime III is 0.0671 and is more than twice the calculated natural St_n for the neutrally buoyant tethered sphere. Interestingly, St_r is almost precisely half of the wake frequency for a fixed sphere at the same Reynolds number of $St = 0.134$. This point is explored further below.

As the Reynolds number is increased through this regime, the radial oscillation frequency is maintained at $St = 0.067$; however, the oscillation moves from radial to
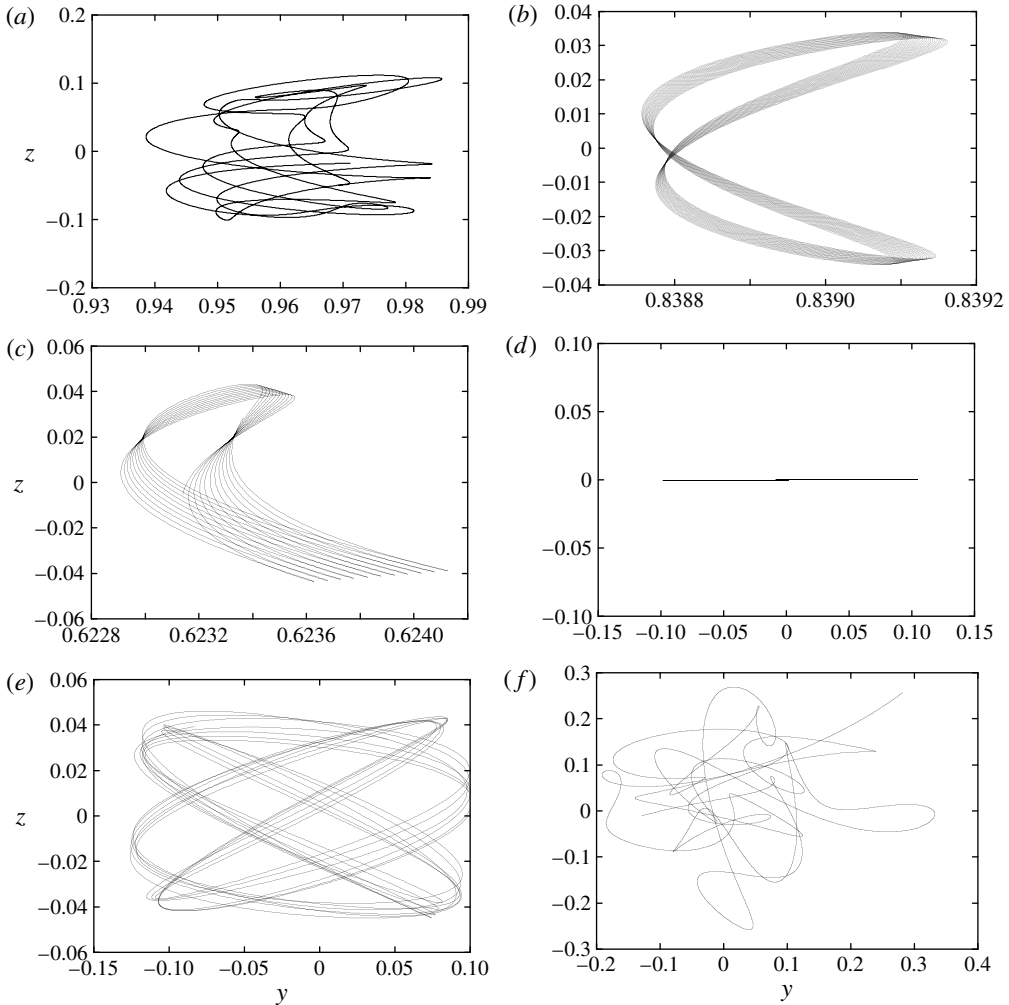
FIGURE 8. Trajectories in the *yz* plane at various Reynolds numbers from the numerical simulations: (*a*) *Re* = 280 (regime III); (*b*) *Re* = 310 (regime IV); (*c*) *Re* = 330 (regime IV); (*d*) *Re* = 450 (regime V); (*e*) *Re* = 500 (regime V); (*f*) *Re* = 800 (regime VI). Note that the axes have quite different scales to show the complex motion of the sphere.

predominantly azimuthal. At *Re* = 280, the azimuthal oscillation is more than four times the radial oscillation amplitude (0.110 : 0.0241) and the azimuthal oscillation frequency is *St* = 0.0214, which is much closer to the natural shedding frequency. The overall oscillation is quasi-periodic. As the Reynolds number is increased further, the radial oscillation amplitude continues to reduce.

By *Re* = 300, the oscillation is almost purely azimuthal. This Reynolds number marks the beginning of regime IV. For this regime, the azimuthal oscillation frequency jumps up to *St* = 0.11, with an amplitude of $A_\theta^* = 0.03$–0.045. The radial oscillation amplitude is very small, but the oscillation frequency is *St* = 0.22, twice the radial oscillation frequency. The *yz* motion in this regime seems to approach a limit cycle – see figures 8(*b*) and 8(*c*). This behaviour is maintained until *Re* = 330.
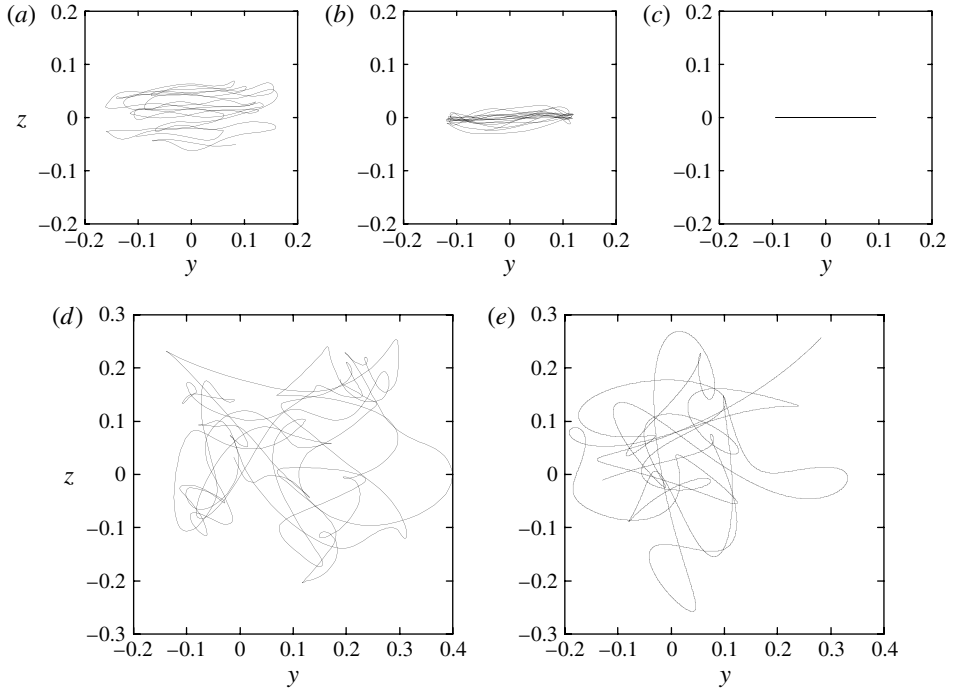
FIGURE 9. A comparison of experimental and numerical trajectories for the Reynolds-number range common to both the experiments and numerical simulations. In regime V: (*a*) experimental trajectory for $Re = 370$; (*b*) experimental trajectory after removing the random drift in mean position with time; (*c*) numerical trajectory for $Re = 400$. In regime VI: (*d*) experimental trajectory for $Re = 815$; (*e*) numerical trajectory for $Re = 800$.

Beyond $Re = 330$, in regime V, the mean position of the sphere is no longer offset from the neutral point. The oscillation initially reverts to purely radial, with an amplitude of $A_r^* = 0.08$–0.12. The radial oscillation frequency is close to constant across this range at $St_r = 0.104$, not far below the Strouhal number of a fixed sphere at onset of shedding at 0.134. At the end of the Reynolds-number range for this regime, azimuthal oscillation returns. Again, the motion appears quasi-periodic, with the complex yz trajectory (see figure 8*e*) appearing close to a limit cycle. The frequency ratio is close to $St_r/St_z \simeq 7/5$.

In regime VI, for $Re > 500$, the vibrations become chaotic and the sphere undertakes chaotic wandering about the neutral point as shown in figure 8(*e*) for $Re = 800$, the highest Reynolds number simulated. The oscillation amplitude varied from $0.2D$ at $Re = 500$ to $0.25D$ at $Re = 800$. Note that these are only approximate because of the chaotic nature of the oscillations.

5.2.1. *Experimental results*

The trajectories in the xy and yz planes at various Reynolds numbers were recorded and were processed as described previously to calculate the time-dependent position of the tethered sphere. The main experimental findings were twofold. First, the existence of regimes V and VI found from the numerical investigations is verified. Figure 9 shows a comparison of experimental and numerical trajectories for regimes V and VI. For regime V, the experimental trajectory (figure 9*a*) is predominantly unidirectional,
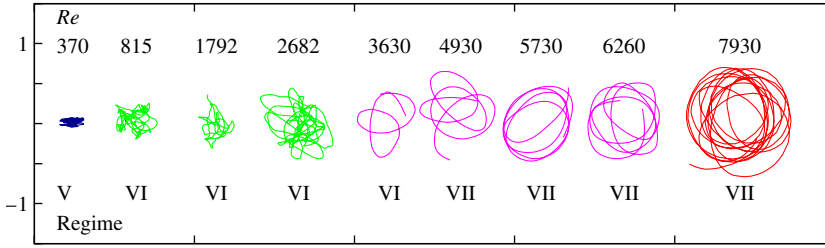
FIGURE 10. (Colour online) Trajectories in *yz* plane from experiments. Both axes have the same scale and are normalized by the sphere diameter *D*.
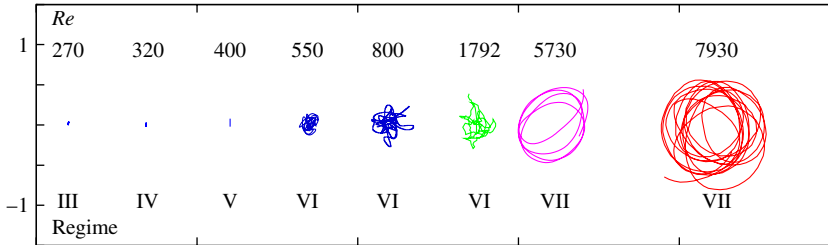

FIGURE 11. (Colour online) Compilation of trajectories in *yz* plane for unsteady regimes. The blue lines (*Re* = 270 to 800) are the numerical results. Again, both axes have the same scale and are normalized by the sphere diameter *D*.

although there is some wandering from one cycle to another, presumably due to low-level background noise in the water tunnel. This random shift in the centre of each orbit with time corresponds to a typical drift speed of the order of 1 % of the free stream velocity. Note that the turbulence level of the water tunnel used for the experiments is approximately 1 %, and hence this slow drift of the centre of each orbit with time is not surprising. It is possible to approximately remove the drift from each orbit by tracking the position of the centre of each orbit of the trajectory as a function of time, fitting a spline and using this to continuously correct the trajectory. The corrected trajectory is shown in figure 9(*b*). This further verifies that the movement is almost linear in the *yz* plane. The numerical trajectory (figure 9*c*) is also purely unidirectional in this regime. For both the experiments and simulations, the amplitude of oscillation is approximately 0.1 diameters. The experimental data gave a Strouhal number of 0.120, which is close to the numerical value of 0.104. For regime VI, the experimental (figure 9*d*) and numerical (figure 9*e*) trajectories show chaotic wandering of similar amplitude about the neutral point on the *x* axis.

Figure 10 shows how the trajectories of the sphere change as the Reynolds number is increased. The orbits shown are obtained from the experiments. The chaotic wandering observed in regime VI increases significantly in amplitude as the Reynolds number is increased up to $Re \simeq 3000$. Beyond this Reynolds number, the trajectories become increasingly elliptical or quasi-circular and increasingly concentric up to the highest Reynolds number considered of $Re = 11\,870$. This new trajectory type is identified as regime VII.

To compare the trajectories and amplitudes of oscillation for each regime, the trajectories in the *yz* plane of the unsteady regimes are shown in figure 11. The

Re	D^*_{circle}	f^*_y	f^*_z
3 630	0.44	0.0293	0.0293
4 930	0.56	0.0335	0.0335
5 730	0.62	0.0352	0.0352
6 260	0.58	0.0360	0.0360
6 432	0.56	0.0310	0.0310
7 418	0.66	0.0347	0.0347
7 930	0.68	0.0397	0.0397
11 870	0.96	0.0454	0.0454

TABLE 2. The diameter of the quasi-circular area and the frequency of oscillation in regime VII from experiments. Here $D^*_{circle} = D_{circle}/D$, and $f^* = fD/U$. Note that the sphere oscillates at a frequency higher than the estimated range of $f^*_n = 0.0145$–0.0214. This is also the case for VIV of a cylinder with $m^* \leqslant 1$.

variation of the oscillation amplitudes shown in figure 5 can be observed in figure 11. This reinforces that the sphere oscillation in the unsteady regimes III to V is close to linear, albeit swapping from radial to azimuthal and then back to radial. The trajectories are chaotic in regime VI, and quasi-circular in regime VII.

The response variables characterizing the sphere oscillation in regime VII are given in table 2. The diameter of the circle (calculated as $D_{circle} = D_y/2 + D_z/2$) gradually grows as Re increases, and reaches about $1D$ at the maximum Reynolds number investigated of $Re = 11\,870$. The diameter of the area enclosed over many orbital cycles is somewhat larger, as can be seen in figure 10 for $Re = 7930$.

The non-dimensionalized natural frequency, f^*_n, calculated using (5.1), is in the range of $f^*_n = 0.0145$–0.0214 for the Reynolds-number range investigated. Only an estimate of f^*_n was possible owing to the lack of force data from the experiments. It is obvious that the sphere oscillates at a frequency higher than its natural frequency in regime VII. A similar frequency response has been reported in the study of VIV of a transversely oscillating cylinder: when $m^* \leqslant 1$, or of the order of unity, the cylinder oscillates at considerably higher frequency than its natural frequency. This (orbital) frequency, however, is lower than that of the other regimes.

5.3. *Vortex structure around the sphere and in the wake*

The vortex structures of the different regimes are shown in figures 12–17. The structures are rendered using isosurfaces of streamwise vorticity (regime II) and also by the λ_2 eigenvalue approach (Jeong & Hussain 1995) for regimes III through VI. Figure 12 shows the vorticity plot of regime II for $Re = 210$. A vorticity plot for regime I is not presented because the steady axisymmetric flow has zero streamwise vorticity. For regime II, the axisymmetry is broken, although the wake remains steady. The wake is characterized by a pair of counter-rotating streamwise vortices, with self-induction causing them to offset from the pivot axis. In turn, this results in a net force causing the sphere also to migrate off the pivot axis. Thus the layover angle decreases away from 90° in this regime.

Regimes III, IV and V consist of periodic shedding of vortices as shown in figures 13–15. Within regime III, the body oscillates initially radially but increasingly azimuthally for increasing Reynolds number. At $Re = 270$, the streamwise vortices of opposite signs do not interact significantly as they pinch off and shed downstream, and vorticity of each sign remains on the same side of the sphere from which it was shed.
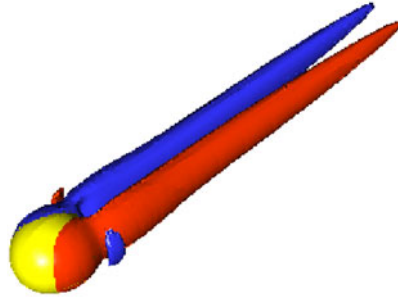
FIGURE 12. (Colour online) Streamwise vorticity of regime II ($Re = 210$) from simulations. Flow is from the bottom left corner to the top right. Positive streamwise vorticity is shown in mid-grey (red online) and negative streamwise vorticity in darker grey (blue online). The vorticity values are ± 0.1, and the two trailing streamwise vortices are apparent.
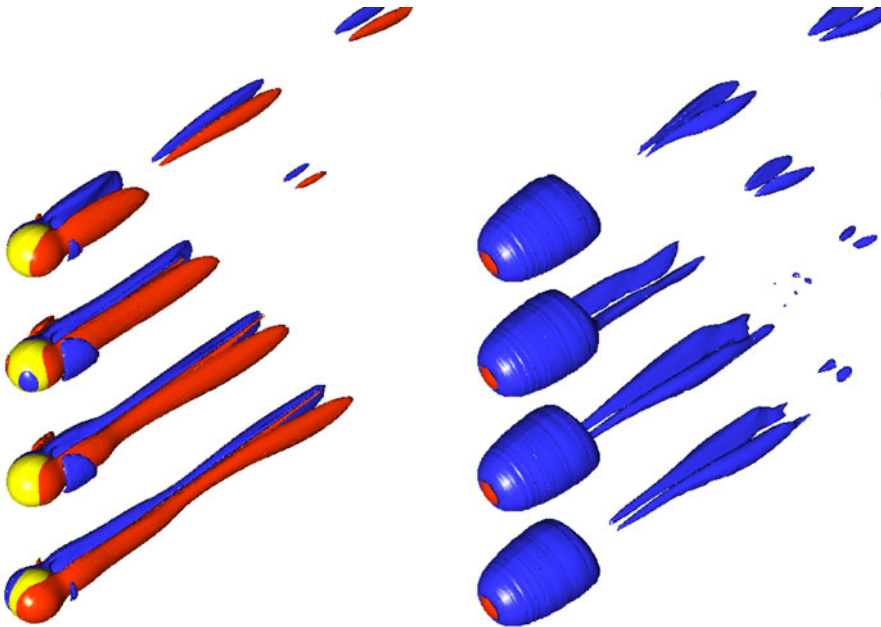

FIGURE 13. (Colour online) Evolution of the corresponding vortical wake structures over a radial oscillation period from the lowest point in the cycle from numerical simulations at $Re = 270$. This corresponds to the start of regime III. Images are separated by one-quarter of a radial oscillation period. The first column shows isosurfaces of streamwise vorticity, and the second column shows the λ_2 field defined by Jeong & Hussain (1995). The grey levels (colours online) for the streamwise vorticity are same as in figure 12. The two-tailed vortical wake is periodically pinched off during the evolution.

The radial oscillation is not purely sinusoidal, but rather modulated, corresponding to inwards and outwards movement over several oscillation cycles, as can be seen from figure 8(*a*). This explains why the shedding over one cycle shown in the figure does not appear to be periodic. As mentioned previously, the radial oscillation frequency of $St_r = 0.0671$ is half the wake shedding frequency for the fixed sphere ($St = 0.134$).
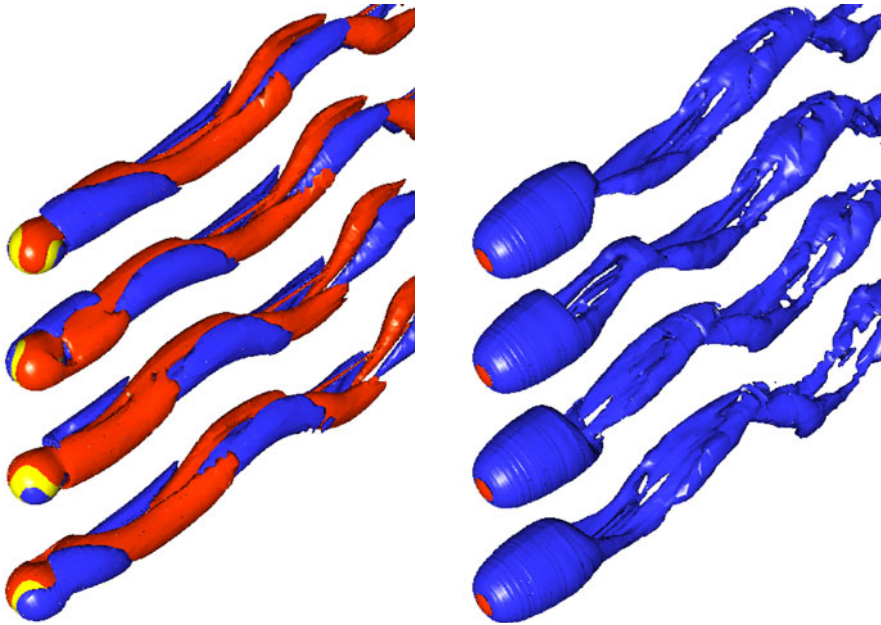
FIGURE 14. (Colour online) Evolution of vortical wake structures for $Re = 330$ (regime IV) (from numerical simulations). The details of the plots are the same as in figure 13. Hairpin-shaped vortex loops appear in the wake.

Indeed, pinching together of the trailing streamwise vortices occurs twice per cycle, even though the vorticity field in the immediate neighbourhood of the sphere varies over a single cycle.

As the Reynolds number is increased in this regime, two things happen. The vibration alters from being radially dominant to being azimuthally dominant. This corresponds with breaking of planar symmetry, allowing flow across the plane passing between the trailing vortices, and also a tendency towards shedding more symmetric vortex loops, i.e. successive loops facing upwards and downwards, rather than facing only one way. The increase in loop symmetry causes a movement of the mean sphere position back towards the neutral point, i.e. the layover angle moves back towards 90°. The breaking of planar symmetry is perhaps more intriguing. For the wake of a fixed sphere, this transition occurs at approximately $Re = 375$ (Mittal 1999*b*), which is much higher than the Reynolds number at which it is seen for the tethered sphere ($Re = 280$). These trends continue as the Reynolds number is increased. By $Re = 300$, the start of regime IV, the oscillation is almost purely azimuthal (but see figures 8*b* and 8*c*) and the azimuthal oscillation frequency has increased and stabilized at $St_\theta = 0.111$. The shedding of loops is not yet symmetric, with the layover angle increasing back towards 90°. Figure 14 shows the vortex shedding pattern at the end of this regime ($Re = 330$). In particular, note that the upward- and downward-facing loops appear to be relatively symmetrical.

At the start of regime V, for $Re > 330$, the layover angle rapidly increases back to 90° and shedding reverts to being radial and centred about the neutral point. This is consistent with the development of a symmetric wake, with upward- and downward-facing vortex loops of equal strength. Figure 15 shows the different depictions of the shedding pattern at $Re = 400$. In addition, planar symmetry returns and is maintained
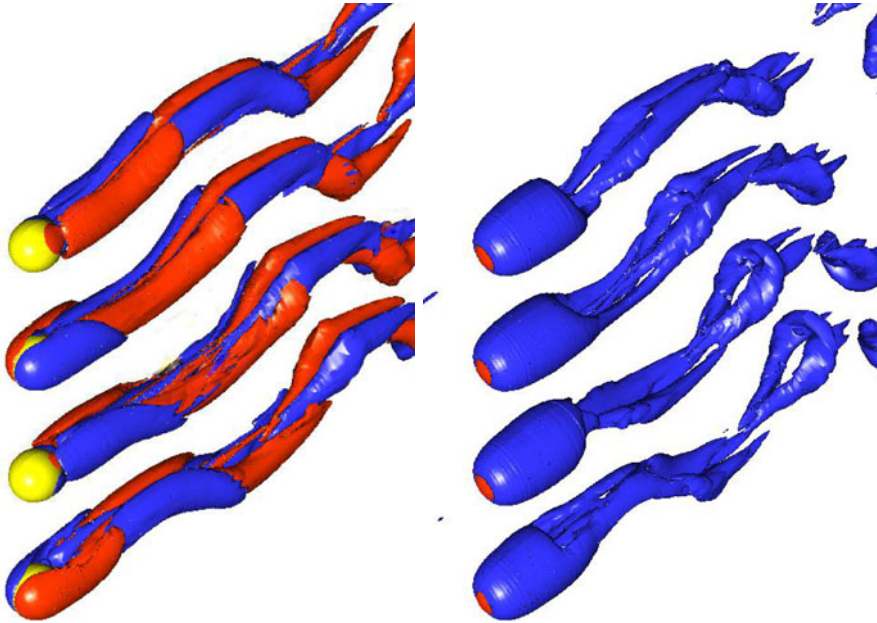
FIGURE 15. (Colour online) Evolution of vortical wake structures for $Re = 400$ (regime V) (from numerical simulations). The details of the plots are the same as in figure 13. The hairpin-shaped vortices are now quite pronounced and maintain planar symmetry.

until at least $Re = 450$. At $Re = 500$, the yz trajectory is no longer linear (see figure 8*e*), indicating once more the loss of planar symmetry.

The motion of the sphere in regime VI ($Re = 700$) shows irregular behaviour, owing to the loss of regular shedding of vortices. In figure 16, the hairpin vortex loops are visible although they are not as apparent as the cases for regimes IV and V. After the flow becomes irregular, the differences in the wake vortex structure are more difficult to characterize.

5.4. *Phase relationship between forces and displacements*

In general, fluid forces are the cause of bluff-body movement when the body is free to move. For VIV, the phase between the fluid force and the displacement helps to explain its response, and hence the dynamics can be investigated by examining phase plots. For the VIV problem, Bearman (1984) pointed out the importance of the phase, together with other parameters such as the mass ratio and structural damping ratio. Many researchers, such as Blackburn & Henderson (1999) and Carberry *et al.* (2004), have interpreted the phase information in terms of the direction of energy transfer between the fluid flow and the body, and have calculated this using phase plots.

For a bluff body under forced vibrations, the energy transfer may be negative, because the body can transfer energy to the fluid flow. However, the energy must be positive for a freely vibrating bluff body, as the body needs to extract energy from the fluid flow to maintain its vibration.

Phase information can also be used to detect a change of response regimes in VIV problems. Bishop & Hassan (1964) were the first to mention this relationship. Govardhan & Williamson (2005) found, for VIV of a transversely vibrating cylinder, that the phase relationships between the vortex force and the displacement, and
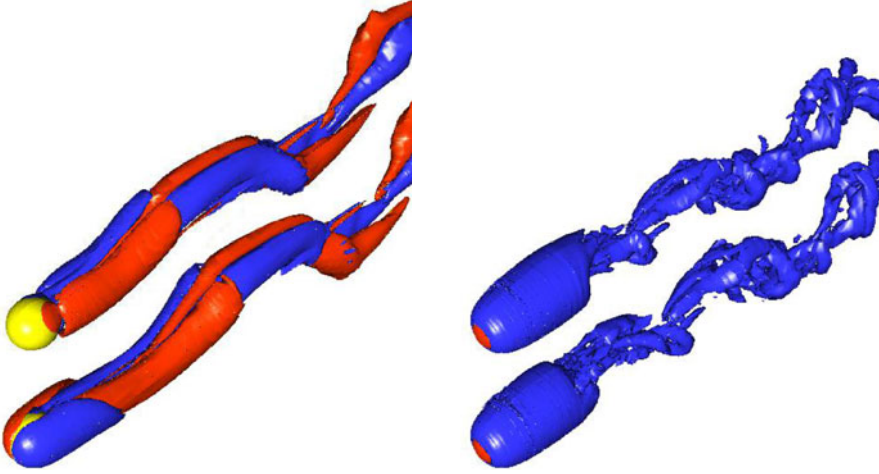
FIGURE 16. (Colour online) Vortex structure at $Re = 700$ (regime VI) at $t^* = 510$ (top) and $t^* = 513$ (bottom) time units. The sphere motion has no periodicity. (Again, these are from numerical simulations.) The details of the plots are the same as in figure 13. The hairpin-shaped vortices are visible, but no longer maintain their planar symmetry.
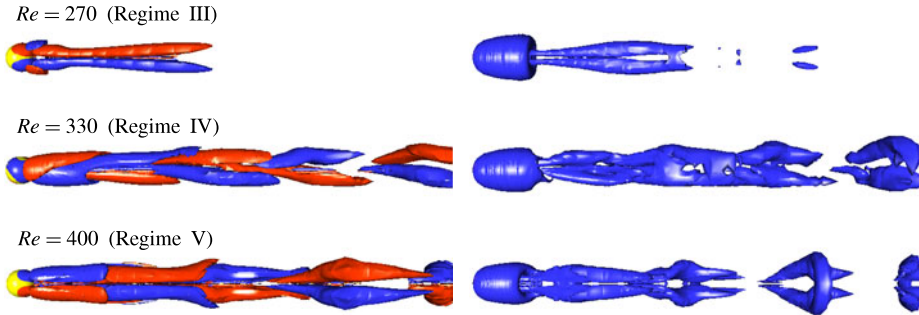

$Re = 270$ (Regime III)

$Re = 330$ (Regime IV)

$Re = 400$ (Regime V)

FIGURE 17. (Colour online) Views in xy plane of the vortex structure at the top position of the cycle in unsteady regimes from numerical simulations. It is clear that the structure is planar-symmetric at $Re = 270$ (regime III) and 400 (regime V). The planar symmetry is lost when $Re = 330$ (regime IV).

the total force and the displacement change when the body goes through the three response branches: the initial, the upper and the lower branches. With this in mind, the phase is plotted and analysed for unsteady regimes (regime III to VI) of the tethered sphere found through numerical simulations. For all three regimes, the total force, pressure force component, viscous force component and displacement are provided for all three Cartesian directions.

The motions in the x, y and z directions are coupled and not independent, owing to the constant tether length ($L^* = 10$). They are related to each other by (5.10), and the sphere moves on a spherical surface defined by L^*, θ and ϕ. As L^* is fixed at $L^* = 10$ for all the simulations considered, the motion is actually two-dimensional in θ and ϕ. However, the following discussions are presented in terms of x, y and z for convenience, considering the initial conditions used in the simulations for the neutrally
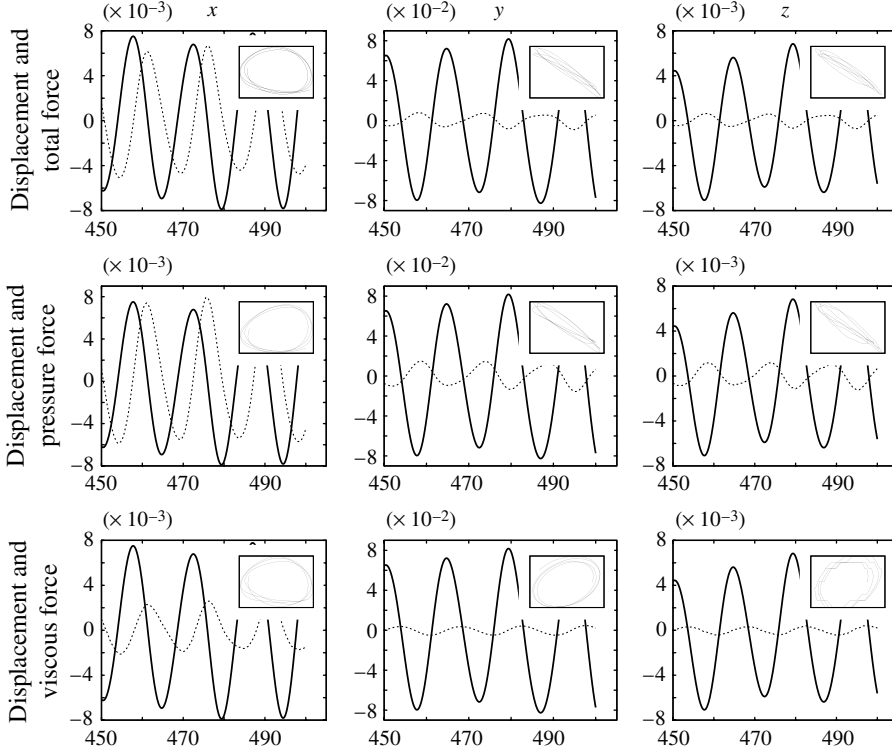
FIGURE 18. History of the displacements (thick solid line) (measured in units of the sphere radius) and the forces (thin dashed line) at $Re = 270$ (regime III). The abscissa of the history is in non-dimensional time units. The insets of each panel are the phase plots between the displacement (abscissa) and the force (ordinate). The axes in the phase plot are auto-scaled to show the pattern more clearly. These data are extracted from the numerical simulations.

buoyant sphere:

$$x = L \cos \theta, \tag{5.8}$$
$$y = L \sin \theta \cos \phi, \tag{5.9}$$
$$z = L \sin \theta \sin \phi. \tag{5.10}$$

When $m^* = 1$, there is no preferred direction in the yz plane, as buoyancy is zero, whereas the sphere oscillates in the z direction when $m^* \neq 1$. For all the following simulations when $m^* = 1$, the initial conditions introduce a perturbation in the y direction; thus, the results show the largest oscillation in the y direction. This is one reason why the following results are discussed in the xyz coordinate system. However, note that the motion of a tethered sphere with a constant-length tether is basically two-dimensional, and there is no preferred direction of oscillation in the cross-flow (yz) plane when the sphere is neutrally buoyant.

In regime III ($Re = 270$), the total fluid force in the x direction as well as its pressure and viscous components lead the x displacement by $\varphi \approx 270°$, as shown in the time histories of the force and the displacement of figure 18. At this value of $\varphi = 270°$, the phase plots are characterized by a circle. In the y direction, only the viscous force component shows the phase value of $\varphi = 270°$. The total fluid force
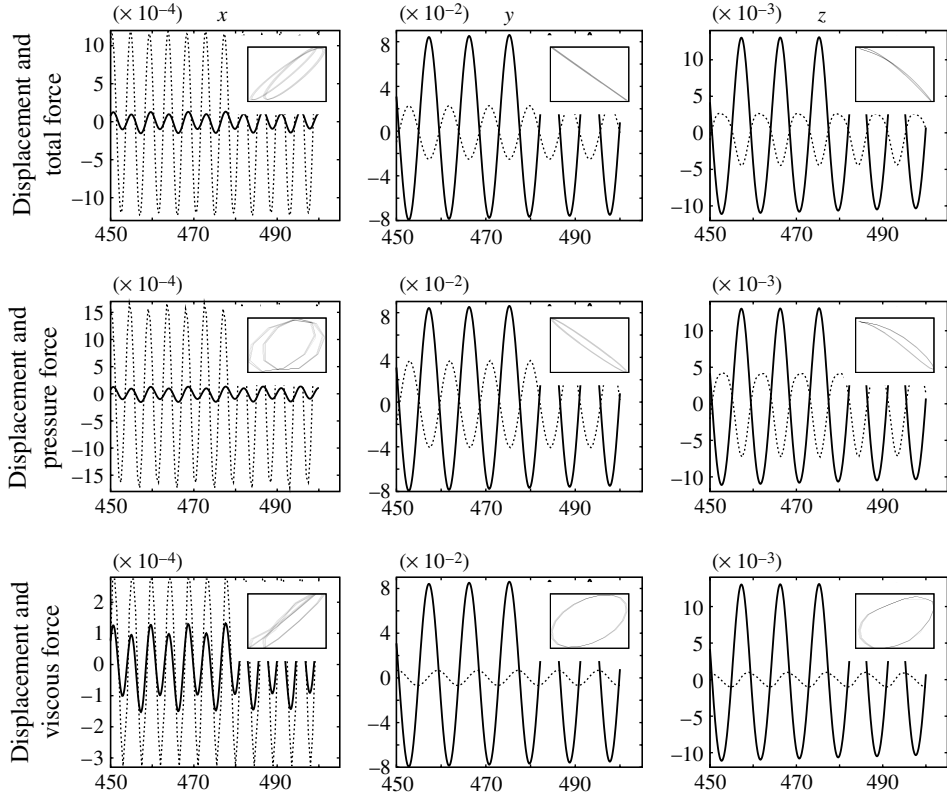
FIGURE 19. History of the displacements (thick solid line) (measured in units of the sphere radius) and the forces (thin dashed line) at $Re = 330$ (regime IV). The abscissa of the history is in non-dimensional time units. The insets of each panel are the phase plots between the displacement (abscissa) and the force (ordinate). The axes in the phase plot are auto-scaled to show the pattern more clearly. These data are extracted from the numerical simulations.

in the y direction and its pressure component show a phase value of $\varphi < 90°$. If $\varphi = 90°$, the phase plot will exhibit a straight line from the top left to the bottom right. It should be noted that the body oscillates mainly in this direction. Although the magnitude of the force and the displacement in the z direction are small, they exhibit the same characteristics as in the y direction, i.e. $\varphi_{F_V-z} \approx 180°$, $\varphi_{F_P-z} \approx 90°$ and $\varphi_{F_{total}-z} \approx 90°$.

The histories of the forces and the displacement, and the phase plots for regime IV ($Re = 330$), are provided in figure 19. In the x direction, the total fluid force and all its components have the phase value $\varphi \approx 0°$. In detail, the phase between the viscous force component and the displacement is $\varphi \approx 360°$ (meaning that the viscous force is slightly behind the x displacement), and $\varphi_{F_{total}-x}$ is closer to zero than φ_{F_P-x}. In the main oscillation direction of y, these two phase values change to 180° (see figure 19). However, $\varphi_{F_V-y} \approx 270°$, similar to that of the x direction as well as that for regime III. A quick look at the phase plots for the other unsteady regimes shows that φ_{F_V-y} and φ_{F_V-z} have almost the same value of 270°. The z fluid force shows non-sinusoidal history, which makes the phase plots distorted, as shown in figure 19. As in the y directional force and displacement, $\varphi_{F_{total}-z} \approx 180°$ and $\varphi_{F_P-z} \approx 180°$.
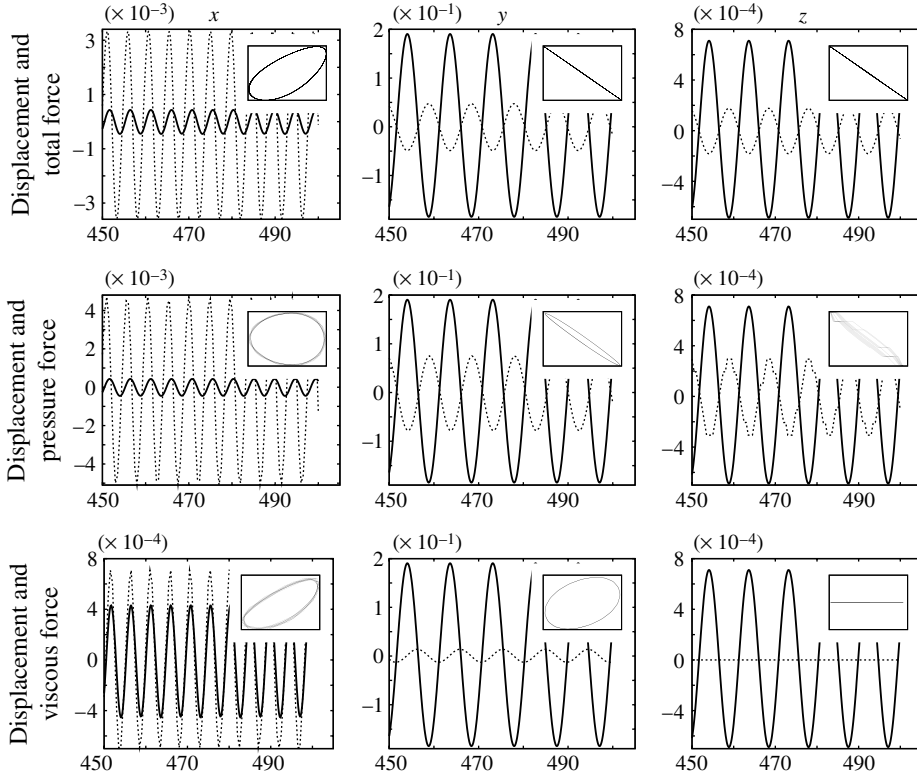
FIGURE 20. History of the displacements (thick solid line) (measured in units of the sphere radius) and the forces (thin dashed line) at $Re = 400$ (regime V). The abscissa of the history is in non-dimensional time units. The insets of each panel are the phase plots between the displacement (abscissa) and the force (ordinate). The axes in the phase plot are auto-scaled to show the pattern more clearly. These data are extracted from the numerical simulations.

Figure 20 shows the histories of the forces and displacement in the x direction for regime V for the specific case of $Re = 400$. In the x direction, the total force advances the displacement with the phase (φ) less than $45°$ and close to the condition of being in phase. If we look at the pressure and viscous components of the total, the phase between the x and the viscous force components is less than that of the x and the pressure force components. Nevertheless, the difference in the value of the phase is very small and both values are less than $90°$. The pressure force component comprises about 90% of the magnitude of the fluctuating x force. This portion of the force component is similar to the forces in the y and z directions, as the sphere is a bluff body. Actually, the oscillation in the x direction is not of interest, owing to its minute oscillation (since it is highly constrained) compared with that of y and z. The sphere oscillates mainly in the y direction. It is obvious that total force and the displacement are out of phase, i.e. $\varphi_{F_{total}-y} \approx 180°$. This is the same for the pressure component, and $\varphi_{F_{P}-y} \approx 180°$. However, for the viscous component, $\varphi_{F_{V}-y} \approx 270°$ as was observed for regimes III and IV.

Figure 21 shows the histories of the forces and displacement when $Re = 500$. Even though this Reynolds number is categorized in regime V (the same regime as $Re = 400$), the oscillation in the z direction appears. The y and z oscillations
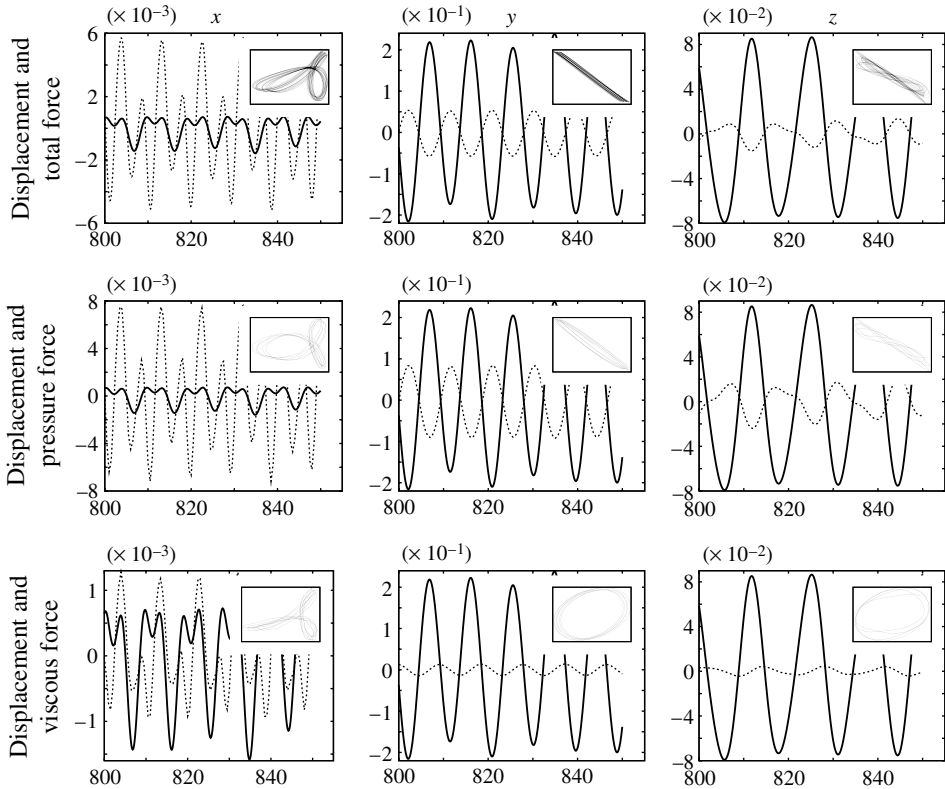
FIGURE 21. History of the displacements (thick solid line) (measured in units of the sphere radius) and the forces (thin dashed line) at $Re = 500$ (regime V). The abscissa of the history is in non-dimensional time units. The insets of each panel are the phase plots between the displacement (abscissa) and the force (ordinate). The axes in the phase plot are auto-scaled to show the pattern more clearly. These data are extracted from the numerical simulations.

are quite periodic at this $Re = 500$, but their trajectories are very different from those of the $Re = 400$ case. Secondary oscillation is clearly observed in the x force and displacement. As a result, the phase plots exhibit a particular shape of limit cycle shown in figure 21 even though the amplitude is small. This is the case for oscillations in both the y and z directions; their histories of displacement and force exhibit secondary (low-frequency) oscillations. Based on the phase plots for the y and z directions, it is indicated that the total force and the corresponding displacement are out of phase. This is the case for the pressure force component for both y and z.

6. Conclusions

This paper examines the VIV response of a neutrally buoyant tethered sphere. Neutral buoyancy represents an interesting special case in that the influence of gravity is excluded, while a long tether allows undamped, almost planar, motion. Experiments and simulations are combined to show that there exist seven different flow regimes in the Reynolds-number range $50 \leqslant Re \lesssim 12\,000$, based on the behaviour of the mean layover angle, amplitude of oscillation, frequency of oscillation and trajectory of oscillation in the cross-flow plane. The first six regimes were determined

by direct numerical simulation and the (sixth and) seventh regimes were found through experiments at higher Reynolds number.

The first regime, regime I, covers the range of $50 \leqslant Re < 210$, with the sphere remaining stationary at a symmetrical layover angle of $\vartheta = 90°$. Regime II covers the range $210 \leqslant Re < 270$. The sphere remains stationary and the flow is steady but non-axisymmetric. The increasing strength of the counter-rotating vortex pair means that the layover angle moves further away from the neutral position at $\vartheta = 90°$ as the Reynolds number is increased.

As Re increases further, the sphere starts to vibrate at $Re = 270$, the start of regime III. Regime IV begins at $Re = 300$. It shows a return of the layover angle back towards $90°$ with increasing Reynolds number as the shed vortex loops become more symmetric. The sphere predominantly oscillates in the azimuthal direction, with a frequency of $St = 0.111$, which is reasonably close to that of the stationary sphere ($St = 0.134$) but much higher than its natural frequency ($St \approx 0.029$).

In regime V, covering $Re = 332$–500, the layover angle returns to $\vartheta = 90°$. In contrast to regime IV, the sphere motion is predominantly in the radial direction. The amplitude of oscillation in regime V gradually increases as Re is increased. The frequency of the radial displacement for regime V is 0.104. This Strouhal number is also close to but still less than that of the fixed sphere ($St = 0.134$). In regime VI, the vibrations become chaotic and the sphere undertakes chaotic wandering. The range of Re for regime VI covers both simulations and experiments, and the existence of the regime is verified by observations of a similar irregular pattern in the experimental visualizations for the overlapping Reynolds-number range.

In regime VII ($Re \geqslant 3000$), the oscillation changes from chaotic wandering to quasi-circular motion. As Re is raised further, the orbits of the sphere exhibit a more clearly circular shape. Table 3 summarizes the seven regimes found for the neutrally buoyant tethered sphere.

Of some interest is the change to the symmetry-breaking transitions relative to the fixed-sphere case. For the wake of a fixed sphere, the initial steady/axisymmetric to steady/non-axisymmetric transition occurs at $Re \simeq 212$, and the next transition from steady/non-axisymmetric flow to unsteady/non-axisymmetric flow occurs at $Re \simeq 272$. These two transitions occur in the same sequence and at the same Reynolds numbers (within numerical uncertainty) as for the tethered sphere. Beyond these Reynolds numbers, there are distinct differences between the wake states once the sphere starts to vibrate. At onset, the radial oscillation frequency $St_r = 0.0671$ is half that for the fixed-sphere case ($St = 0.134$); however, pinching together of the trailing streamwise vortices occurs twice per cycle. By $Re = 280$, the oscillation has switched to be predominantly azimuthal rather than radial. This is associated with the loss of symmetry in the wake with respect to the plane running between the trailing vortices. Breaking of planar symmetry only occurs for the fixed sphere at $Re = 375$. Planar symmetry remains broken for the tethered sphere in regimes IV and V, but it is recovered in regime VI from $Re > 330$ and maintained until at least $Re = 450$.

As indicated in the introduction, Provansal *et al.* (2004) observed quasi-circular motion of a sphere with $m^* = 2.433$ in an experimental study of a vertically tethered sphere. They observed quasi-circular or elliptic motion in the plane normal to the flow for $Re = 600$–800. In addition, from numerical simulations, Behara *et al.* (2011) found circular oscillations for an $m^* = 2$ elastically mounted sphere with three degrees of freedom at $Re = 300$ for $4 \leqslant U^* \leqslant 9$. Both of these findings contrast with the sphere response seen in experiments presented here, as this circular motion appears only at much higher Reynolds numbers of $Re > 3000$. The substantial difference in

Regime	Reynolds number	Trajectory	Wake characteristics
I	$50 \leqslant Re < 210$	N/A	Steady, axisymmetric
II	$210 \leqslant Re < 270$	N/A	Steady, non-axisymmetric, planar-symmetric, 'double-thread' wake vortex formation
III	$270 \leqslant Re < 300$	Radial, shifting to azimuthal	Unsteady periodic, planar-symmetric, start of periodic vortex shedding
IV	$300 \leqslant Re < 332$	Primarily azimuthal	Unsteady periodic, no planar symmetry, periodic vortex shedding in the form of vortex loops
V	$332 \leqslant Re < 550$	Linear radial	Unsteady periodic, planar-symmetric, periodic vortex shedding in the form of vortex loops
VI	$550 \leqslant Re < 3000$	Irregular	Unsteady non-periodic, vortex shedding pattern becomes irregular
VII	$3000 \leqslant Re < 12\,000$	Quasi-circular	Unsteady periodic, helix-shaped vortex formation without shedding

TABLE 3. Regimes of the flow and response of the neutrally buoyant tethered sphere for the range of $Re = 50$–$12\,000$. The trajectories are those of the oscillating sphere on the cross-flow (yz) plane.

mass ratio for those two cases from the one examined here may help explain the different trajectories. In addition, the numerical results of Behara *et al.* (2011) used springs in all three directions to control the motion rather than a tether, allowing full three-dimensional movement, whereas the tether restricts the motion of the sphere to lie on a two-dimensional spherical surface. Also, the restoring force of the tether is approximately quadratic from the neutral point, while springs are linear. Finally, the reduced velocity ranges are substantially different. Using a tether to supply a restoring force does not allow independent variation of the reduced velocity; it lies in the relatively narrow range $34 \leqslant U^* \leqslant 44$, as the Reynolds number is varied between the onset of shedding at $Re = 270$ up to $12\,000$. The use of springs to provide the restoring force allows the reduced velocity to be varied independently. Thus Behara *et al.* (2011) chose a reduced velocity range for which resonance is likely between the structural and the wake frequencies. To investigate the different response a little further, limited simulations were undertaken with the flow direction aligned with gravity, and for a mass ratio of $m^* = 2.433$, in line with the study of Provansal *et al.* (2004). The simulations indeed showed that the cross-plane trajectories became approximately circular for $Re \gtrsim 500$, consistent with their results.

REFERENCES

BEARMAN, P. W. 1984 Vortex shedding from oscillating bluff bodies. *Annu. Rev. Fluid Mech.* **16**, 195–222.

BEHARA, S., BORAZJANI, I. & SOTIROPOULOS, F. 2011 Vortex-induced vibrations of an elastically mounted sphere with three degrees of freedom at $Re = 300$: hysteresis and vortex shedding modes. *J. Fluid Mech.* **686**, 426–450.

BISHOP, R. E. D & HASSAN, A. Y. 1964 The lift and drag forces on a circular cylinder in a flowing fluid. *Proc. R. Soc. Lond.* A **277**, 51–75.

BLACKBURN, H. M. & HENDERSON, R. D. 1999 A study of two-dimensional flow past an oscillating cylinder. *J. Fluid Mech.* **385**, 255–286.

BRÜCKER, C. 2001 Spatio-temporal reconstruction of vortex dynamics in axisymmetric wakes. *J. Fluids Struct.* **15**, 543–554.

CARBERRY, J., GOVARDHAN, R., SHERIDAN, J., ROCKWELL, D. & WILLIAMSON, C. H. K. 2004 Wake states and response branches of forced and freely oscillating cylinders. *Eur. J. Mech. (B/Fluids)* **23**, 89–97.

CHOMAZ, J. M., BONNETON, P. & HOPFINGER, E. J. 1993 The structure of the near wake of a sphere moving horizontally in a stratified field. *J. Fluid Mech.* **254**, 1–21.

DENNIS, S. C. R. & WALKER, J. D. A. 1971 Calculation of the steady flow past a sphere at low and moderate Reynolds numbers. *J. Fluid Mech.* **48**, 771–789.

GHIDERSA, B. & DUŠEK, J. 2000 Breaking of axisymmetry and onset of unsteadiness in the wake of a sphere. *J. Fluid Mech.* **423**, 33–69.

GOTTLIEB, D. & ORSZAG, S. A. 1977 *Numerical Analysis of Spectral Methods: Theory and Applications*. SIAM.

GOTTLIEB, O. 1997 Bifurcations of a nonlinear small-body ocean-mooring system excited by finite-amplitude waves. *Trans. ASME: J. Offshore Mech. Arctic Engng* **119**, 234–238.

GOVARDHAN, R. & WILLIAMSON, C. H. K. 1997 Vortex-induced motions of a tethered sphere. *J. Wind Engng Ind. Aerodyn.* **69–71**, 375–385.

GOVARDHAN, R. & WILLIAMSON, C. H. K. 2005 Vortex-induced vibrations of a sphere. *J. Fluid Mech.* **531**, 11–47.

GRIFFIN, O. M. & RAMBERG, S. E. 1982 Some recent studies of vortex shedding with application to marine tubulars and risers. *Trans. ASME: J. Energy Resour. Technol.* **104**, 2–13.

HARLEMANN, D. & SHAPIRO, W. 1961 The dynamics of a submerged moored sphere in oscillatory waves. *Coast. Engng J.* **2**, 746–765.

JAUVTIS, N., GOVARDHAN, R. & WILLIAMSON, C. H. K. 2001 Multiple modes of vortex-induced vibrations of a sphere. *J. Fluids Struct.* **15**, 555–563.

JEONG, J. & HUSSAIN, F. 1995 On the identification of a vortex. *J. Fluid Mech.* **285**, 69–94.

JOHNSON, T. A. & PATEL, V. C. 1999 Flow past a sphere up to a Reynolds number of 300. *J. Fluid Mech.* **378**, 19–70.

KARNIADAKIS, G. E., ISRAELI, M. & ORSZAG, S. A. 1991 High-order splitting methods of the incompressible Navier–Stokes equations. *J. Comput. Phys.* **97**, 414–443.

KARNIADAKIS, G. E. & TRIANTAFYLLOU, G. S. 1992 Three-dimensional dynamics and transition to turbulence in the wake of bluff objects. *J. Fluid Mech.* **238**, 1–30.

KIM, H. J. & DURBIN, P. A. 1988 Observations of the frequencies in a sphere wake and of drag increase by acoustic excitation. *Phys. Fluids* **31** (11), 3260–3265.

LEE, H., THOMPSON, M. C. & HOURIGAN, K. 2008 Vortex-induced vibrations of a tethered sphere with neutral buoyancy. In *Proceedings of the XXIIth International Congress on Theoretical and Applied Mechanics (ICTAM 2008), Adelaide, Australia*, p. 11299.

LEONTINI, J. S., THOMPSON, M. C. & HOURIGAN, K. 2007 Three-dimensional transition in the wake of a transversely oscillating cylinder. *J. Fluid Mech.* **577**, 79–104.

LEWEKE, T., PROVANSAL, M., ORMIÈRES, D. & LEBESCOND, R. 1999 Vortex dynamics in the wake of a sphere. *Phys. Fluids* **11** (9), S12.

LEWEKE, T., THOMPSON, M. C. & HOURIGAN, K. 2006 Instability of the flow around an impacting sphere. *J. Fluid Struct.* **22** (6), 961–971.

MAGARVEY, R. H. & BISHOP, R. L. 1961*a* Transition ranges for three-dimensional wakes. *Can. J. Phys.* **39**, 1418–1422.

MAGARVEY, R. H. & BISHOP, R. L. 1961*b* Wakes in liquid–liquid systems. *Phys. Fluids* **4**, 800–805.

MITTAL, R. 1999*a* A Fourier–Chebyshev spectral collocation method for simulating flow past spheres and spheroids. *Intl J. Numer. Meth. Fluids* **30**, 921–937.

MITTAL, R. 1999*b* Planar symmetry in the unsteady wake of a sphere. *AIAA J.* **37**, 388–390.

MORISON, J. R., O'BRIEN, M. P., JOHNSON, J. W. & SCHAAF, S. A. 1950 The force exerted by surface waves on piles. *Petrol. Trans. AIME* **189**, 149–157.

NATARAJAN, R. & ACRIVOS, A. 1993 The instability of the steady flow past spheres and disks. *J. Fluid Mech.* **254**, 323–344.

ORMIÈRES, D. & PROVANSAL, M. 1999 Transition to turbulence in the wake of a sphere. *Phys. Rev. Lett.* **83**, 80–83.

PRASAD, A. & WILLIAMSON, C. H. K. 1997 The instability in the shear layer separating from a bluff body. *J. Fluid Mech.* **333**, 375–402.

PREGNALATO, C. J. 2003 The flow-induced vibrations of a tethered sphere. PhD thesis, Monash University, Melbourne, Australia.

PROVANSAL, M., SCHOUVEILER, L. & LEWEKE, T. 2004 From the double vortex street behind a cylinder to the the wakes of a sphere. *Eur. J. Mech. (B/Fluids)* **23**, 65–80.

RYAN, K., THOMPSON, M. C. & HOURIGAN, K. 2007 The effect of mass ratio and tether length on the flow around a tethered cylinder. *J. Fluid Mech.* **591**, 117–144.

SARPKAYA, T. 1979 Vortex-induced oscillations. *Trans. ASME: J. Appl. Mech.* **46**, 241–258.

SARPKAYA, T. 1986 Force on a circular cylinder in viscous oscillatory flow at low Keulegan–Carpenter numbers. *J. Fluid Mech.* **165**, 61–71.

SARPKAYA, T. 2004 A critical review of the intrinsic nature of vortex-induced vibrations. *J. Fluids Struct.* **19**, 389–447.

SCHOUVEILER, L. & PROVANSAL, M. 2002 Self-sustained oscillations in the wake of a sphere. *Phys. Fluids* **14**, 3846–3854.

SHI-IGAI, H. & KONO, T. 1969 Study on vibration of submerged spheres caused by surface waves. *Coast. Engng Japan* **12**, 29–40.

STEWART, B. E., THOMPSON, M. C., LEWEKE, T. & HOURIGAN, K. 2010 Numerical and experimental studies of the rolling sphere wake. *J. Fluid Mech.* **643**, 137–162.

TANEDA, S. 1956 Experimental investigation of the wakes behind cylinders and plates at low Reynolds numbers. *J. Phys. Soc. Japan* **11**, 302–307.

THOMPSON, M. C. & HOURIGAN, K. 2005 The shear layer instability of a circular cylinder wake. *Phys. Fluids* **17** (2), 021702.

THOMPSON, M. C., HOURIGAN, K., CHEUNG, A. & LEWEKE, T. 2006 Hydrodynamics of a particle impact on a wall. *Appl. Math. Model.* **30** (11), 1356–1369.

THOMPSON, M. C., HOURIGAN, K. & SHERIDAN, J. 1996 Three-dimensional instabilities in the wake of a circular cylinder. *Exp. Therm. Fluid Sci.* **12**, 190–196.

THOMPSON, M. C., LEWEKE, T. & HOURIGAN, K. 2007 Sphere–wall collision: vortex dynamics and stability. *J. Fluid Mech.* **575**, 121–148.

THOMPSON, M. C., LEWEKE, T. & PROVANSAL, M. 2001 Kinematics and dynamics of sphere wake transition. *J. Fluids Struct.* **15**, 575–585.

TOMBOULIDES, A. G. & ORSZAG, S. A. 2000 Numerical investigation of transitional and weak turbulent flow past a sphere. *J. Fluid Mech.* **416**, 45–73.

TOMBOULIDES, A. G., ORSZAG, S. A. & KARNIADAKIS, G. E. 1993 Direct and large-eddy simulation of axisymmetric wakes. *AIAA Paper* 93-0546..

WILLIAMSON, C. H. K. 1988 The existence of two stages in the transition to three-dimensionality of a cylinder wake. *Phys. Fluids* **31**, 3165–3168.

WILLIAMSON, C. H. K. & GOVARDHAN, R. 1997 Dynamics and forcing of a tethered sphere in a fluid flow. *J. Fluids Struct.* **11**, 293–305.

WILLIAMSON, C. H. K. & GOVARDHAN, R. 2004 Vortex-induced vibrations. *Annu. Rev. Fluid Mech.* **36**, 413–455.